Simulation of Cortical Electric Fields during Deep Brain Simulation (DBS)

Thesis Report

Master Assignment Electrical Engineering

Course code: 191211219

Amal Reji
s2991950
MSc Electrical Engineering
Biomedical Signals and Systems
University of Twente
Enschede, the Netherlands

August 24, 2024

Examination Committee

Committee Chair: dr.ir. T. Heida (Ciska)
Supervisors: dr.ir. B.C. Schwab,
dr.rer.nat. M.C. Piastra
Daily Supervisor: T. Keizers MSc
External Supervisor: dr.ir. J.T.W. Berendsen

UNIVERSITY OF TWENTE.

Contents

List of Figures

List of Tables

1 Acknowledgements

I express my sincere gratitude and thanks to everyone who has contributed and helped in the completion of my Master assignment at the Biomedical Signals and Systems (BSS) research group at the University of Twente. This opportunity has been very valuable and a great learning experience for me to delve into the field of electromagnetics and brain simulations. I owe a great deal of its success to the help and encouragement of many people from the BSS research group, the University of Twente, and the Brain stimulation lab with people with years of experience. I am thankful for the opportunity to collaborate with such accomplished individuals with years of experience who have not only motivated me but also added a genuine joy to my master assignment.

First, I would like to thank Prof. DR.IR. B.C. Schwab (Bettina), Associate Professor, University of Twente, for providing me this opportunity to work on the deep-brain simulations under her guidance. I would also like to thank DR. RER. NAT. M.C. (Maria Carla) Piastra, assistant professor in the Clinical Neurophysiology (CNPH) group, University of Twente, for providing her valuable insight and guidance on the assignment.

I am very grateful to Thomas Keizers, PhD candidate for the Desynchronizing Weak Cortical Fields during Deep Brain Stimulation [DECODE] project under Prof. Bettina for guiding me through my thesis. His expertise and guidance helped me explore different ways of approaching a problem and provided me with a clear view on the ways to approach my research question. This enabled me to continue learning while maintaining my attention on the intended outcome within the allotted time.

In addition, I want to express my gratitude to my family and friends, whose support has been a constant source of inspiration for me. Their confidence in my skills has motivated me to complete this assignment successfully.

2 Abstract

Background : Deep Brain Stimulation (DBS) is an established treatment for patients with neurological and psychiatric conditions. Traditionally, DBS has focused on the strong electric fields generated near the electrode site in subcortical regions. However, weak electric fields, which are less intense and extend further away from the stimulation site into cortical regions, are also present and may influence treatment outcomes. Noninvasive brain stimulation techniques, such as transcranial current stimulation (tCS), have shown that these weak fields can modulate brain activity effectively, suggesting that the weak fields generated during DBS could also play a significant role in treatment outcomes. The DESYNCHRONIZING WEAK CORTICAL FIELDS DURING DEEP BRAIN STIMULATION (DECODE) project investigates the impact of these weak fields on neural activity during DBS. This study, part of the DECODE project, aims to develop a general head model for DBS simulations to quantify and compare the electric field magnitude and distribution in cortical regions.

Objective : To quantify and investigate the strength and spatial distribution of electric fields in the cortical regions for monopolar and bipolar configurations during deep brain stimulation when using the Medtronic 3389 lead implanted in the subthalamic nucleus (STN).

Methods : The electric field distribution was calculated using a numerical method with a realistic head model, incorporating Medtronic 3389 DBS leads. Multiple toolboxes were used to gather data for the model creation. Mesh generation was performed with Iso2Mesh, and cortical parcellations were obtained from FreeSurfer. The simulations were carried out using FEMfuns with an input current of 2 mA. The electric field and parcellation data were subsequently post-processed to obtain an electric field for cortical regions.

Results : Monopolar simulations generate electric fields with mean magnitudes ranging from 0.0154 V/m to 0.2556 V/m and maximum values up to 3.13 V/m, with contact 3 showing the highest mean magnitude of the electric field, ranging from 0.0173 V/m to 0.2556 V/m and maximum values up to 3.13 V/m. In bipolar simulations, the mean magnitude of the electric field varies between 0.001 V/m and 0.12 V/m, with maximum values up to 1.94 V/m. Within bipolar configurations, simulations 2 and 4 show the highest mean magnitude of the electric field, with values ranging from 0.001 V/m to 0.12 V/m, and maximum electric field values up to 1.9373 V/m.

Conclusion : Monopolar configurations influence more cortical regions, while bipolar configurations offer more targeted stimulation within the cortical regions. The findings show that monopolar configurations, particularly with contact 3, generate stronger and more widespread electric fields than bipolar configurations, which produce more localized fields. The results highlight that varying contact positions significantly influence the electric field's magnitude and distribution, with contact 3 in monopolar configuration and specific cathode-anode pairings in bipolar setups offering optimal stimulation conditions. Notably, the mean magnitudes of electric fields generated within the cortical regions by both monopolar and bipolar DBS configurations are within the same order of magnitude as those produced by other noninvasive brain stimulation techniques. However, the maximum electric fields within the cortical regions generated by DBS are one order of magnitude, or slightly more, higher than the maximum electric fields produced by tCS.

Keywords: Deep brain stimulation, Electrodes, Monopole, Dipole, Monopolar Simulation, Bipolar Simulation, Mesh, Electromagnetics, Monopolar/Bipolar Electric potential, Monopolar/Bipolar Electric field, FEMfuns, FEniCS, SimNIBS, Normal Components of Electric Fields, Cortical Parcellation,

3 Abbreviations

DBS - Deep Brain Stimulation

STL - Stereolithography

CG - Continuous Galerkin

DG - Discontinuous Galerkin

ASCII - American Standard Code for Information Interchange

PDEs - Partial Differential Equations

CG in solvers - Conjugate Gradient

GMRES - Generalized Minimal Residual

ILU - Incomplete LU factorization

AMG - Algebraic Multigrid

EF - Electric Field

LFP - Local Field Potentials

D-Leads - Directional Leads

VTA - Volume of Tissue Activation

NIBS - Non-Invasive Brain Stimulation

NIfTI - Neuroimaging Informatics Technology Initiative

TLE - Temporal Lobe Epilepsy

4 Introduction

4.1 Deep Brain Stimulation

Deep Brain Stimulation (DBS) is a therapeutic method for the intervention of neurological and psychiatric conditions such as Parkinson's Disease, epilepsy, essential tremor, and dystonia. DBS is performed in individuals for whom pharmacological interventions alone no longer have the desired effect, fail to manage their motor symptoms effectively, or cause unwanted side effects. It is not suitable for everyone, patients must function well cognitively and should not have a balance disorder. It is an invasive method that uses stereotactic neurosurgical techniques to implant electrodes (leads) inside the brain. DBS delivers chronic electrical simulation from the electric pulses generated from the lead which modulates the neuronal activities. These effects are dependent on the pulse width, rate, and amplitude of the pulse generated in the lead [5]. The lead pulses are controlled by a neurostimulator surgically implanted below the clavicle or abdomen. During surgery, leads are placed on one side or both (unilateral or bilateral), depending on the need for treatment. They are placed based on the region to be stimulated and the number of leads is also decided based on the area of interest. The electrical stimulations from the lead influence neurons in the brain by inducing a pattern of activation and inhibition of neurons near the lead[6].

DBS has been introduced to provide a better quality of life for patients with neurological disorders, with a focus on movement disorders and Parkinson's Disease (PD). It is effective in controlling tremors due to PD that are refractory to dopaminergic drugs, motor fluctuations, and levodopa-induced dyskinesia [5], essential tremors, and tremors due to multiple sclerosis. Studies show that DBS has improved disease symptoms such as reduced tremors in patients with dyskinesia and an increase in quality of life in patients with PD by up to 50 percent. For PD, common targets for lead implantation are the subthalamic nucleus (STN) or the globus pallidus (GP), specifically the globus pallidus internus [7]. Studies have also shown that DBS could be used in younger patients [8]. When comparing PD treatment for quality of life, daily activities, and duration of dyskinesia with medication treatment from multiple randomized control trials, the results demonstrate notable improvements. Specifically, compared to medication treatment, the alternative intervention led to a 26 percent improvement in quality of life, a 30 percent enhancement in daily activities, and a 20 percent reduction in the duration of dyskinesia [8]. In the case of primary dystonia, DBS has been used to stimulate the internal segment of the globus pallidus in patients with medication-refractory dystonia and has shown long-term efficacy [9]. DBS has also been used as a treatment for obsessive-compulsive disorder and comorbid depression. The stimulation was carried out in the nucleus Accumbens and the Caudate nucleus, which showed a slight improvement, and the stimulations in the ventral capsule showed a clinical improvement of 50 percent of the patients[8]. DBS is also used as a treatment for temporal lobe epilepsy (TLE) with a common target of the Hippocampus to reduce seizures in patients. Short-term randomized control trials have shown that DBS can reduce seizures by up to 15 percent and long-term randomized control trials have been shown to reduce seizures by up to 50 percent in patients with TLE [10].

Many factors determine the good and proper functioning of DBS, including patient selection, placement of leads, and programming of the neurostimulator to send the appropriate signals [5]. Generally, DBS pulses are square wave pulses with an amplitude of 1 to 5V or 0.5 to 10 mA [11, 12, 13], with a duration of 30 to 450 ms, and the values are optimized according to individual patients [8]. Currently, the clinical standard for deep brain stimulation (DBS) involves delivering open-loop, constant-rate stimulation at frequencies greater than 100 Hz, typically between 130 and 180 Hz, with preset amplitude and pulse duration [14]. Local field potentials (LFP) can

be recorded from implanted leads and are believed to reflect synaptic currents in neuronal elements close to the recording site [7]. Placement of the leads has a crucial clinical impact on the short-term and long-term periods as it localizes the electric fields in the head. The leads are selected based on the specific neurological treatment and should consider factors such as patient screening, target selection, flexibility of programming, and patient-specific factors[15]. Conventional DBS leads vary depending on the number of contacts on the lead. The number of contacts varied from four to eight cylindrical contacts and variable inter spacing spanning a vertical distance of 7.5 to 15.5 mm from the tip of the electrode [16],[17]. The contacts of conventional leads can simulate the surrounding tissues radially and distribute the current uniformly in all directions. Recent advancements in DBS have introduced directional leads (D-Leads) which are designed to adapt the volume of stimulation relative to the position within the target by horizontal and vertical current steering directions [17]. The prototypes for the directional leads have varied designs. Some have up to 40 small circular contacts, each about 0.8 mm in size, evenly spaced over the last 5 to 6 mm of the electrode. Other, simpler models divide conventional ring contacts into 3 to 4 segments, each spanning about 90 ° to 120 ° [16],[18]. The design of D-Lead allows for more targeted stimulation by enhancing the contacts to direct the currents more precisely toward the targeted regions. The Medtronic 3389 lead is a conventional DBS lead that has been widely implanted in patients with various neurological diseases. It has been used extensively in numerous clinical studies, demonstrating its efficacy and reliability in deep brain stimulation therapy [19, 17, 20, 21, 22]. The contacts of Medtronic 3398 lead have a height of 1.5 mm, 0.5 mm spacing, and 1.27 mm in diameter. Figure 1 shows the Medtronic 3389 lead.

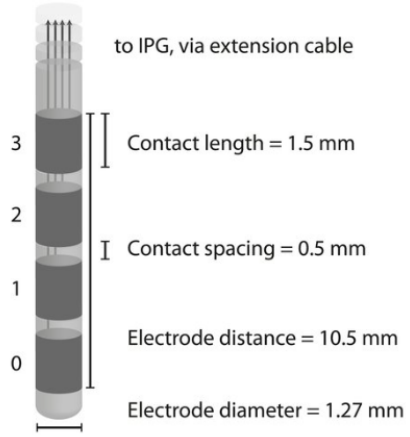

Figure 1: The Medtronic 3389 deep brain stimulation electrode originally published in J.Kahan et al. [1]. The contacts of the lead are numbered from 0 to 3

The orientation of the lead is also a crucial factor that significantly affects the effectiveness of stimulation. Proper orientation of the lead is necessary to target the specified region of the brain to optimize the therapeutic outcome. To ensure the proper orientation of the lead, advanced imaging techniques, and real-time monitoring are used for the navigation and placement of the leads. Studies have shown that precise placement and orientation of the lead can enhance the efficacy of DBS in treating neurological conditions such as Parkinson's disease and dystonia [23, 24].

Depending on the clinical requirements and possible outcomes, the simulations are classified mainly into monopolar and bipolar configurations. In complex cases, dual-target DBS (DT-DBS), with leads placed in both the STN and the GP, may be used to maximize therapeutic

benefit [7]. In the monopolar configuration, one or more electrode contacts are configured as the anode (negative) against the implantable pulse generator, while in a bipolar configuration, at least one contact is activated as the anode, and at least one is activated as the cathode (positive) from the electrode contacts [25].

DBS provides clinical effects by generating pulses from one or more contacts. Monopolar and bipolar stimulation are two methods used in DBS to stimulate the brain. Monopolar stimulation (with anode / negative electrode contact in the brain and cathode / positive contact in the pulse generator) involves the delivery of electrical current from single or multiple active contacts on the DBS electrode to a return electrode placed elsewhere in the body or on the device casing [26]. In monopolar stimulation, the electrical current flows from the active contact through the surrounding tissue, influencing neural activity in the region around the active contact. It is often used in clinical settings to target broader regions of the brain and modulate neural circuits associated with various neurological disorders [26]. They can provide broader and localized stimulation to specific brain regions, allowing a wider modulation of neural activity and relief of symptoms in patients with neurological disorders. Bipolar stimulation (with the anode and cathode contacts in much closer proximity, both within the brain) involves delivering electrical current between two adjacent active contacts on the DBS electrode, creating a field between the two contacts where neural modulation occurs. Electrical current flows between the two active contacts, affecting neural activity in the region between the contacts and potentially delivering less current to the brain region compared to monopolar stimulation [26]. Bipolar stimulation is used to modulate neural circuits in a more spatially controlled manner compared to monopolar stimulation, allowing for different patterns of neural activation and potentially different therapeutic effects [27]. Monopolar stimulation, where the stimulation contacts are spread more widely compared to bipolar stimulation, results in a larger Volume of Tissue Activation (VTA). VTA is defined as the region of space in which neural activity is actively induced or triggered by electrical stimulation. In monopolar setups, the broader spacing of contacts leads to a more extensive VTA compared to the more localized effect seen in bipolar stimulation [26]. Figure 2a shows the distribution of electric potential for a monopolar configuration. The blue region illustrates an anode, and the red region represents a neutral charge. The cathode is located far away from the anode. Figure 2b illustrates the electric potential distribution of the bipolar configuration. The blue region shows the anode and the red region shows the cathode.

Most of the studies conducted in DBS focus on the stimulation site where the neuronal response to the high electric field is strong. Stimulations also induce electric fields to other brain regions that have reduced electric field strength because they are not close to the electrode site. These electric fields of reduced strength are referred to as weak electric fields. Other brain stimulations such as transcranial direct/alternating current stimulation (tDCS/tACS) have sparked significant interest in this low-magnitude electric fields due to its outstanding potential to offer novel non-invasive therapies for neurological disorders [28, 29, 30, 31]. This raises the question whether similar effects could be observed with DBS. Weak electric fields, though present during DBS, have not been thoroughly investigated. This prompts the question of whether the weak electric fields in the cortical region during DBS could influence the treatment's efficacy.

The DESYNCHRONIZING WEAK CORTICAL FIELDS DURING DEEP BRAIN STIMULATION (DECODE) project aims to explore how DBS weak fields affect the brain's neural activity. Traditionally, fields near the electrode site have been the focus because of their strong influence on neural activity. However, research in non-invasive brain stimulation suggests that weaker fields may also play a critical role in treatment effectiveness. These fields might subtly affect neural activity, which could be crucial for long-term success. Understanding these

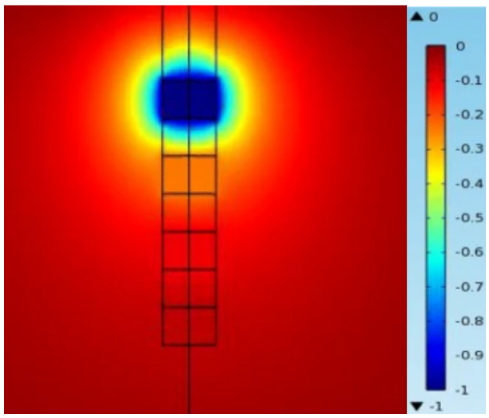

(a) Electric potential distribution at contacts for a monopolar configuration. The cathode is placed far away from the lead and the anode (blue) is one of the contacts on the lead.

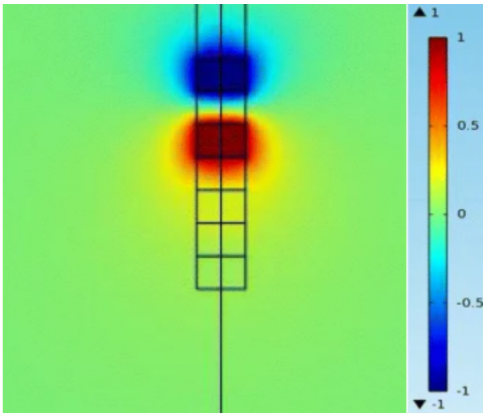

(b) Electric potential distribution at contacts for a bipolar configuration. The cathode is given at one contact (red) and the anode is an adjacent contact (blue).

Figure 2: Figure illustrates the distribution of Electric potential at contacts of the lead for monopolar and bipolar configurations. This figure was originally published in K A Sathi et al. [2]. The axis on the right of the images shows the scale for the magnitude of electric potential in Volts (V)

weaker fields could lead to better therapeutic outcomes and reduced side effects, enhancing treatment for Parkinson's disease and other disorders treated with DBS. Parkinson's disease fundamentally involves motor-neuron problems caused by the degeneration of neurons in specific brain regions, including those in the Cortico-basal ganglia-thalamocortical loop. This loop is essential for motor control and sensory processing, connecting the thalamus and the cerebral cortex. Investigating the distribution of the electric field within the thalamocortical loop can help understand the impact of these weaker electric fields on PD. The electric field distributions during DBS within the cortical regions have not been extensively studied. The main objective of the study is to quantify and investigate the influence of monopolar and bipolar stimulation settings in the electric field generated during DBS and to quantify the electric field strength in the cortical regions during stimulation at different contacts using Finite Element Model (FEM).

4.2 Existing toolboxes

Before implanting the DBS leads, simulations using various FEM programs can be very beneficial. These simulations allow for a comprehensive understanding of DBS functionality, the distribution of electric fields, and the modulation of brain activity. FEM models can be used to simulate the forward problem of volume conduction to calculate the electric potential from which its derivatives can be obtained from post-processing. FEM toolboxes are used because they can be used to simulate geometries like the human brain and to find solutions for equations at every point in the geometry. They can accurately represent anisotropic conductivities, which are crucial for modeling the directional properties of brain tissues. This allows for a more realistic simulation of how electric fields propagate through different brain regions. By quantifying volume conduction, FEM helps us understand how electrical signals distribute throughout the brain tissue, which is essential for effective DBS planning. Additionally, FEM can simulate extracellular potentials, providing insights into the electrical environment outside neurons and its influence on neural activity. The flexibility of FEM models enables customization and adjustment of simulations to fit the specific anatomies and treatment scenarios of individual patients, enhancing the precision and effectiveness of DBS. In FEM, the geometries are created using small elements such as triangles or tetrahedra, and solutions are calculated at nodes or

centroids depending on the problem. There are a variety of FEM software to simulate the brain. An example of FEM is FEMfuns [3], an open-source pipeline to stimulate extracellular potentials and explicitly incorporate electrode properties used for this study.

There are a variety of toolboxes available for brain simulations. Several MATLAB and Python toolboxes, such as SimNIBS, FieldTrip, and FEMfuns, are widely used to set up and run brain simulations. However, some toolboxes, like Iso2Mesh and Lead-DBS, primarily assist in the setup of simulations rather than running them. Even though there are a variety of toolboxes, each of them has its own limitations when trying to simulate DBS. Most of the toolboxes developed are for noninvasive brain simulations such as SimNIBS and FEMfuns. Notably, there isn't a FEM toolbox that can both set up and execute DBS which is why this study uses different toolboxes to run the simulations used for this study. This study uses SimNIBS, Lead-DBS, Iso2Mesh, FreeSurfer, and FEMfuns. A brief background and the use of these toolboxes are given below.

4.2.1 Lead-DBS

Lead-DBS is an open-source FEM software utilized for conducting Deep Brain Stimulation (DBS) procedures. Its purpose is to aid in both the planning and execution of DBS surgeries by integrating various data sources, including imaging data and electrophysiology recordings. This integration improves the accuracy of electrode placement in the brain, which is crucial for successful outcomes. Lead-DBS facilitates the display of high-resolution atlas imaging data, microelectrode localization, Microelectrode Recording (MER) feature extraction, patient-specific imaging, and stereotactic planning information [32]. Lead-DBS uses patient-specific data to tailor the surgical approach and optimize the outcome of DBS. It helps with precision targeting, positioning and customized treatment as brain anatomy varies from person to person. When postoperative data are needed, it helps make decisions by revealing how well the surgery worked and what needs to be changed to get the best possible outcome for the patient. Postoperative data are crucial because they allow medical professionals to assess the true impact of the DBS technique, track patient reaction, and decide whether additional adjustments or therapies are necessary. Treu et.al [20] discuss DBS imaging research at the group level using Lead-DBS. The paper highlights how important electrode positioning is in DBS treatment and how this affects clinical results. The paper emphasizes the creation of specialized software tools that allow researchers to do group studies on DBS imaging, such as Lead-DBS and Lead groups. These instruments have been used in numerous investigations to look at the connection between stimulation sites, anatomical structures, and clinical results in a variety of disorders, including Tourette's syndrome, essential tremor, dystonia, epilepsy, and Parkinson's disease. Supplementary material for the study was given that included the data set used for lead-DBS. The data set included preoperative and postoperative data for 51 PD patients. The implanted lead data from one of the patients is used for this study. The extraction of the leads was done using Lead-DBS. The STLs of the leads that included the contacts and insulation were extracted and used to generate mesh for the leads. Lead-DBS cannot be used to run simulations, which is why other methods were utilized for simulations.

4.2.2 SimNIBS

SimNIBS (Simulation of Non-Invasive Brain Stimulation) is an open-source software package primarily used for computational modeling and simulation of non-invasive brain stimulation (NIBS) techniques, such as transcranial magnetic stimulation (TMS) and transcranial electric stimulation (tES) which intends to provide researchers and clinicians with a tool to accurately

model and predict the effects of NIBS on the human brain [33]. It can be used to create patient-specific head models from MRI data and simulate NIBS. The design takes into account meshing and finite-element computations using open-source tools and integrating other free software packages like FreeSurfer and FSL tools for magnetic resonance (MR) image segmentation. SimNIBS provides example datasets for running simulations, which can be used when patient data is not available. The Ernie dataset is the open-source MR dataset provided by SimNIBS was used for this study. Initially, SimNIBS generates a tetrahedral head mesh using subject-specific T1-weighted and, optionally, T2-weighted MR data. It can readily specify electrode shapes and sizes, evaluate and alter tissue conductivities, allow tDCS simulations with multiple independently controlled electrodes, and copy and modify simulations. SimNIBS was used for this study to generate masks for the head regions from T1-weighted MR images provided in the sample dataset.

The older versions of SimNIBS used the headreco function, which reconstructs a tetrahedral head mesh from T1 and T2 weighted MR images. It can generate a head mesh with just a T1 weighted MR image but with a T2w image, it helps to achieve better segmentation. headreco function is based on SPM12 and CAT12. Statistical Parametric Mapping (SPM12) and Computational Anatomy Toolbox (CAT12) are software suites that analyze functional and structural brain imaging data, primarily from MRI scans. Image preprocessing activities, including segmentation (partitioning the images into different tissue types such as gray matter, white matter, and cerebrospinal fluid) and realignment (correcting for motion artifacts), are frequently performed using these. These toolboxes help in better segmentation of the head model to achieve better head mesh. The headreco output provides tetrahedral head mesh and segmentations for each layer (masks) as STL and NIFTI files which can be used further for post-processing but mainly focuses on getting the main five segments which are skin, skull, cerebrospinal fluid (CSF), gray matter (GM), and white matter (WM) [34].

The newer version of SimNIBS has a function called CHARM [34] which replaces the headreco function. CHARM has shown relatively good segmentation accuracy over all tissues, with higher accuracy on larger structures and lower accuracy on smaller structures. The output of CHARM does not provide masks for different segments. Headreco is not available as it has been deprecated. For this study, an older version of SimNIBS - 2.3.6 was used in order to run headreco. The headreco was preferred over CHARM because the output will have masks for each segment, which can be used for generating a volumetric head mesh for this study. Since the electrode has to be inserted inside the head model for this study, and none of the toolboxes listed above could achieve this, the head mesh had to be generated independently, this will be covered in more detail in the methods section 6.

4.2.3 FreeSurfer

FreeSurfer is an open-source software package designed for the visualization and analysis of structural, functional, and diffusion neuroimaging data. FreeSurfer can generate detailed cortical reconstructions from magnetic resonance imaging, including segmenting white matter and reconstructing the cortical surface, which is essential for measuring cortical thickness. It also provides automatic labeling of subcortical brain structures, facilitating detailed volumetric analysis [35]. It is capable of doing surface-based registration, which aligns cortical surface models to a standard anatomical space for cross-subject comparisons. The function of FreeSurfer in generating detailed cortical reconstruction through surface-based statistical analysis is used in this study to obtain the statistics of cortical parcellations of the head model used for this study. It has the function recon-all, which can be used to obtain the cortical parcellations from T1

weighted MR image. Freesurfer provides cortical parcellation registered to three atlases which are Desikan-Killiany cortical atlas, Destrieux cortical atlas, and DKTatlas 40. These atlases have different numbers of parcellated regions and other differences in the subcortical regions. Desikan-Killiany atlas has 34 regions per hemisphere, Destrieux atlas has 74 regions per hemisphere, and DKT40 has 62 regions per hemisphere [36, 37, 38]. The parcellated data can be selected from three different atlases, depending on the specific requirements of the study.

4.2.4 Iso2Mesh

The volumetric meshing was carried out using the open-source toolbox called Iso2Mesh [39]. It is a MATLAB/Octave-based open-source toolbox developed by Qianqian Fang at Northeastern University's Department of Bioengineering. Its objective is to generate high-quality 3D surface and volumetric meshes from 3D volumetric images. Using Iso2Mesh, researchers and engineers can create meshes from different types of medical imaging data, including MRI and CT scans [40, 41]. It has different functions to generate surface or volumetric meshes from binary, segmented, or grayscale images. Since the data from SimNIBS had binary volume data and STL files, Iso2mesh was used for mesh generation. It has a Computational Geometry Algorithms Library (CGAL) Surface Mesh Generation library, a large set of tools designed to produce well-shaped surface meshes from three-dimensional input data. The resulting surfaces are processed with different smoothing algorithms to provide accurate boundary definitions. A full-head tetrahedral mesh is created using the TetGen utility with constrained Delaunay tetrahedralization [40]. This process allows for control of the mesh density and element quality. By taking a set of points and constraints as input, this method ensures that no point lies inside the circumsphere of any tetrahedron. The resulting tetrahedral elements have well-shaped structures, which are essential for accurate simulations. Additionally, the "constrained" aspect of this method ensures that specific edges and faces, such as anatomical boundaries, are preserved in the mesh. TetGen efficiently handles even complex geometries, providing accurate and reliable meshes that are well-suited for various applications, including medical imaging, engineering simulations, and computer graphics. As a result, these meshes accurately represent the input geometry while maintaining high-quality element shapes.

4.2.5 FEniCS - Legacy Dolfin

Legacy Dolfin refers to an older version of the dolfin component within the FEniCS project. FEniCS is an open-source toolbox that can be used to solve PDEs using the finite element method. It is widely used in academic and industrial settings for research and engineering applications. FEMfuns, the software used for simulations in this study, uses Dolfin functions to run simulations. A detailed explanation of FEMfuns' functionality will be provided in Section 4.3. This section, however, focuses on introducing some of the fundamental functions and terminology associated with legacy Dolfin, which are essential for running FEMfuns.

Function Space
Function spaces are mathematical structures that consist of a set of functions and certain properties which are fundamental in the analysis and solving of PDEs in FEM. Some function spaces used in FEMfuns are given below.

1. **Continuous Galerkin (CG)**: This function space consists of a piecewise linear function within each element of the mesh and is continuous across the boundaries. This means that at any given point in the mesh, functions can be expressed as a linear combination of spatial coordinates of the mesh. For a CG function space, the function values match the shared boundaries in a mesh making it contionus across the boundaries. So for a

function u in CG space, each cell u(x) will be a linear polynomial. At boundaries, u(x) is continuous, so any two elements with a shared boundary will have the same value for u, at the boundary. The solutions found for this function space are found at the nodes of the mesh. In this study, we use the CG function space with order one denoted by CG1.

2. **Discontinuous Galerkin (DG)** : This is a function space that has a piecewise constant for all the cells within it. This means that each cell will have a constant which is defined at the centroids of each cell. For an element k, the function u(k) = c. They can be discontinuous at the boundaries. Since all cells have a constant value, the values can jump from one element to another at the boundaries depending on the properties of each domain in the mesh. In this study, we use the DG function space with order zero denoted as DG0.

3. **Vector Function Spaces**: These are function spaces whose elements are vector values. They can be used to approximate or store vector quantities. In FEM, vector function spaces are constructed by combining scalar function spaces for each component of the vector.

Projection and Interpolation
Projection and interpolation are two fundamental operations for handling and manipulating functions stored in function spaces. These operations are essential for transferring functions and expressions between different function spaces. They are used for representing functions within a finite element framework.

1. **Projection**: It is used to project a given function or expression onto a specified finite element function space. This operation is useful when you need to approximate a function or an expression within a finite element space, as an intermediate step, or for visualization. It resolves a variational problem to project an expression into a function space. It can handle more general expressions, including those involving derivatives or other differential operators. It is denoted by **project**.

2. **Interpolation**: It is used to interpolate a function or expression into a specified finite element function space. Interpolation is the process of approximating a function at the nodes of the finite element mesh, providing a more direct representation of the function within the space. It can be used for directly evaluating expressions that do not involve differential operators or for providing initial conditions. It is denoted by **interpolate**.

Solvers
Solvers are used to find the solutions to the linear and nonlinear systems of equations that arise from the discretization of PDEs. FEniCS provides several types of solvers to handle different types of problem, including direct solvers, iterative solvers, and solvers for nonlinear problems. For solving the Maxwell equation, linear solvers are used. FEMfuns uses iterative solvers that approximate the solution through an iterative process where each iteration gives a solution close to the actual solution. Common iterative solvers include Conjugate Gradient (CG), Generalized Minimal Residual (GMRES), and Bi-Conjugate Gradient Stabilized (BiCGStab). Krylov solvers are a subset of iterative solvers that use Krylov subspace methods to solve large, sparse linear systems. Krylov solver is used by FEMfuns to approximate the solutions. Krylov methods required for FEMfuns are the following.

1. **Conjugate Gradient (CG)**: It is an iterative algorithm for solving linear systems of equations where the matrix is symmetric and positive definite. The method is particularly effective for large and sparse systems. The conditions for CG are A = A^T, which defines it

as symmetric, and $x^T Ax > 0$ which defines it as positive definite. CG method iteratively refines the solution vector x to approximate the true solution of Ax=b. For each iteration, it minimizes the quadratic form in the search direction.

2. **Generalized Minimal Residual (GMRES)**: It is an iterative algorithm for solving general (not necessarily symmetric or positive-definite) linear systems of equations. It is particularly useful for large, sparse, and non-symmetric matrices. It aims to solve the linear system Ax=b by iteratively minimizing the residual. The residual at the m-th iteration is given by

$$r_m = b - Ax_m$$

It minimizes the euclidean norm

$$\|r_m\| = \|b - Ax_m\|$$

over the Krylov subspace $\mathcal{K}_m(A, b)$.

Preconditioners
Preconditioners are used in iterative solvers to improve convergence rates. They modify the original system into a format that is more manageable for the iterative solver. The preconditioned system should ideally have better spectral properties, resulting in quicker convergence. The preconditioners used in FEMfuns are ILU (Incomplete LU) and AMG (Algebraic Multigrid).

1. **Incomplete Lower-Upper (ILU)**: ILU is a preconditioning technique that approximates the LU factorization by selectively ignoring some of the nonzero entries (fill-ins) to maintain the sparsity pattern of the original matrix. This serves as an approximation and saves computational time. They are effective for small-scale problems and, to some extent, higher-order problems, but cannot be used for highly complex problems.

2. **Algebraic Multigrid (AMG)**: AMG is a sophisticated preconditioning technique that uses a multilevel approach to solve linear systems. It uses different levels of resolution to capture both fine and coarse details of the solution. At each level, it uses an iterative method to reduce the errors in the current approximation. The residuals are transferred to a coarser grid which can solve the problem faster at a lower resolution. After the solution is found on the coarser grid, the solutions are transferred back to the finer grid which makes it useful to use in complex computations.

The software mentioned in this section cannot set up and run DBS simulations. The main challenge lies in generating a volumetric mesh of the head model with the lead incorporated inside it. These toolboxes lack the capability to create such a mesh. SimNIBS can create a mesh but with fixed electrode types, while Lead-DBS and FreeSurfer do not have the functionality to create a mesh and simulate, which is why we use FEMfuns for this study. The key advantage of using FEMfuns is that it allows for the integration of a separately created geometric model, which can then be used for simulations. Additionally, FEMfuns enable the assignment of input current based on specified coordinates. The contacts obtained from Lead-DBS along with the output STL files from SimNIBS were used to create the volumetric head model using Iso2mesh. This volumetric mesh is used for simulations in FEMfuns. The detailed process of mesh generation is provided in the Methods section 6.2.

4.3 FEMfuns

FEMfuns is a Python-based open-source volume conduction pipeline for solving forward problems. It enables the simulation of electric potential distributions in volume conductors gener-

ated by known sources, providing a versatile platform for modeling various geometrical domains, source configurations, and electrode properties, including both resistive and capacitive materials. It uses legacy dolfin. Using advanced FEM techniques within the FEniCS framework, it accurately solves partial differential equations (PDEs) that govern the electric potential in complex neural tissue environments. For precise simulations, the pipeline offers electrode-electrolyte implementations and adaptive refinement options. The process of simulating a system includes several steps, including mesh creation, definition of simulation parameters (source type, tissue properties, electrode interface), execution of FEM simulation, and visualization of results. FEMfuns solves the PDE for the mesh given as input. It also provides flexibility in including subdomains and interior and exterior boundary conditions to represent electrodes and different types of point sources and incorporate electrode properties [42]. The initial input to FEMfuns is the XML files for the mesh and its physical and facet region after the conversion from gmsh (finite element mesh generator) using FEniCSs Dolfin-convert.

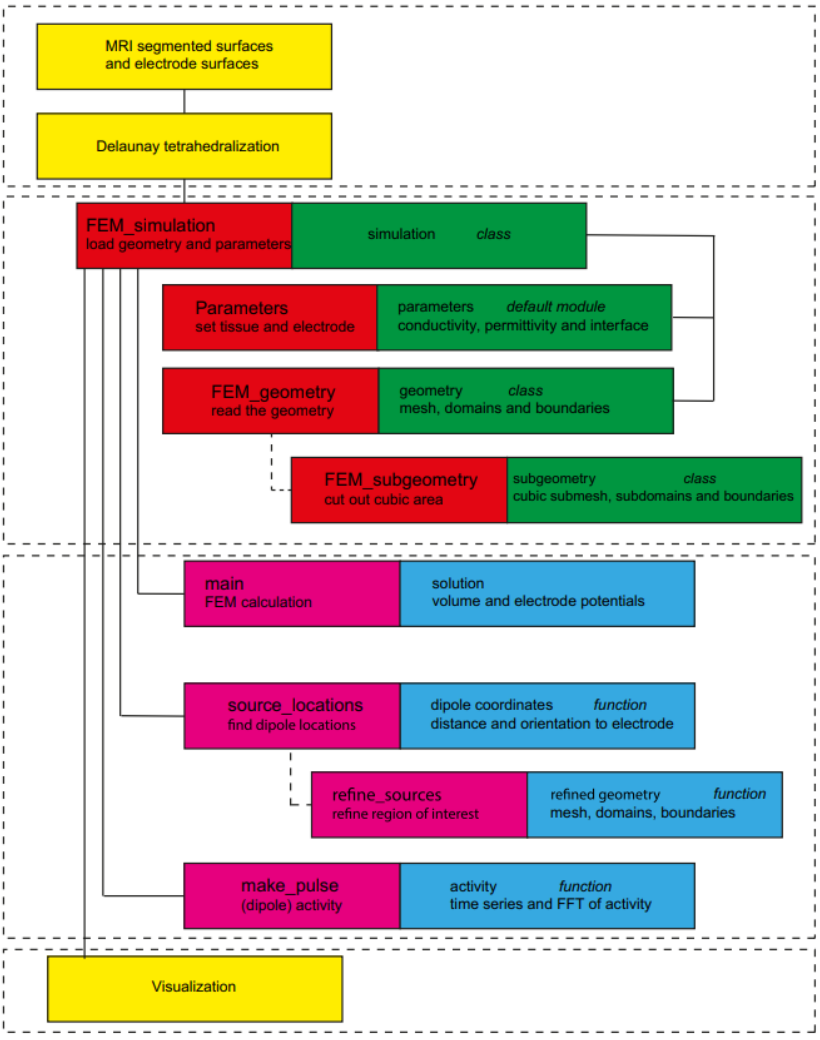

Figure 3: Workflow of FEMfuns (Originally published in Vermaas et al., 2020) [3].

Figure 3 illustrates the workflow of FEMfuns. The solutions for each cell in the mesh were found using FEniCS. In the forward model, the aim is to simulate the distribution of electric potentials in the head model resulting from electrode stimulation. The potentials at each cell

inside the mesh are found by solving for φ in Poisson's equation given by

$$-\nabla.(\sigma\nabla\varphi) = \nabla J_p \textbf{ in } \Omega \text{ for resistive medium} \tag{1}$$

The electric potential generated is represented as φ, Ω represents the medium, ∇ is the gradient operator, and J_p represents the primary current density. On the external boundary, a homogeneous Neumann boundary condition (BC) is used for simulation denoted by :

$$\sigma\nabla\varphi.\mathbf{n} = 0 \text{ on } \partial\Omega \tag{2}$$

where n is the unit vector on the domain, implying the unit normal to the surface is zero.

Electric fields propagate through tissues much faster than neural activity, which typically occurs at frequencies ranging from a few to hundreds of Hertz in the brain. The model streamlines the analysis without sacrificing accuracy by assuming quasistatic conditions, where the electric fields shift slowly over time compared to the frequency making equations easier to solve computationally. The quasistatic approximation is commonly used in neurophysiological studies such as EEG and ECoG, for various reasons, including its ability to simplify complex models and enhance computational efficiency.

FEniCS is used to solve PDEs by dividing them into simpler elements or cells. The process of finding a solution contains two major steps :
1. Weak formulation
2. Discretization

The initial step is to derive the weak formulation of the PDE that governs φ. FEniCS uses two functions called test and trial functions. Trial functions are the approximations of the unknown solution of the PDE which represents the linear combination of basis functions defined over each element in the subdomain. The coefficients of the trial function are the unknowns to be determined. The weak formulation is achieved by multiplying the PDE by a test function v and integrating over the domain V ($v \in V$), leading to an equation that involves the unknown electric potential and its derivatives. The weak formulation is taken in the FEM due to its mathematical advantages, including the ability to handle boundary conditions, facilitate integration by parts, ensure convergence properties, provide variational principles, offer flexibility in function spaces, and promote numerical stability in solving complex PDEs.

The next step involves the discretization of the weak form of PDE to generate the linear system of equations which involves approximating the continuous problem by dividing the domain into smaller elements, and the solution is approximated using piecewise continuous basis functions defined on these elements as a finite linear combination of basis functions[3]. The output from FEMfuns is the electric potential generated at the nodes of the cells within the mesh. The calculated potential can be used to post-process the data. This is why FEMfuns was chosen for this study. FEMfuns has not been previously used for simulating DBS but it was used for noninvasive brain simulations, but it has the potential to run DBS. FEMfuns can integrate separately created mesh and assign the currents based on specified coordinates. This helps in using a head model incorporated with leads and assigning the currents based on the coordinates of the lead to run DBS. FEMfuns provide electric potential distribution for the given mesh after assigning parameters which helps to get the data after running DBS.

5 Aim of the study and Research question

Limited studies have been conducted on monopolar and bipolar simulations in the context of DBS with a focus on the distribution and strength of electric fields in cortical regions, thus emphasizing the necessity of further investigation. Thus, the aim of the study is to quantify and investigate how monopolar and bipolar simulations, as well as varying the contact positions for stimulation on the lead influence the strength and distribution of electric field in the cortical regions. Simulations are done for a generic head model by taking the lead position from open-source Lead-DBS post-operative data from PD patients, where the leads are implanted in the STN. Initially, a simulation setup has to be created by meshing the head with leads implanted in the desired orientation as this is not present for any existing toolboxes. This is then used to simulate DBS. Detailed simulations are conducted by assigning current sources to all contacts of the Medtronic 3389 lead contacts simultaneously to compare the effect of simulation at different contacts for monopolar and bipolar configurations. The comparison of the simulations is carried out by analyzing the magnitude of the electric field, the normal components of the electric field, and their visualization. Visualization is performed for the entire head model and for the cortex. This study aims to improve the understanding of how different DBS setups can be optimized to maximize efficiency. Thus, the main research question for this study is:

- **How do monopolar and bipolar configurations impact the strength and distribution of electric fields in the cortical regions during deep brain stimulation (DBS) when using the Medtronic 3389 lead implanted in the subthalamic nucleus (STN)?** Specifically, in terms of the quantification of the electric field strengths, quantification of the normal components of the electric field, and spatial characteristics when using the Medtronic 3389 lead implanted in the subthalamic nucleus (STN), based on a dataset derived from a Parkinson's disease (PD) patient? And the sub-questions are :
  - **How do simulations with varying contact positions within the DBS lead affect the strength and distribution of electric fields in the cortical regions?** This analysis investigates how different lead contact placements, by individually simulating each contact, can affect the magnitude and normal components of electric fields, and their spatial distribution.
  - **How do monopolar and bipolar simulations with varying contact positions within the DBS lead affect the magnitude of the weak electric field in the cortical regions?**

Based on previous studies [5, 26, 12, 43, 44, 2], we hypothesize that monopolar simulations have a higher magnitude of electric field and a wider distribution compared to bipolar simulations. Not a lot of studies were found on the influence of varying contact positions on the electric field distribution for the specific lead model. Studies are being conducted for the comparison of electric fields for different leads, but not by varying the contacts of the same lead. It was hypothesized that simulating at contact 3 would have better strength and distribution for monopolar configurations. This was taken as contact 3 will have the maximum distance from the cathode compared to other contacts. In addition, as contact 3 for the lead is the furthest from the subcortical regions, it has the potential to generate more magnitude of weak electric field so it is hypothesized that monopolar configuration simulating at contact 3 would have a higher magnitude of weak electric field.

6 Methods

This section presents a detailed explanation of the data collection process, mesh generation, simulation, and post-processing of the data from the simulation for further analysis.

6.1 Data Collection

Creating a head model including the DBS lead was the first step in the study. The volume data of the masks can be retrieved from the Neuroimaging Informatics Technology Initiative NIfTI(nii) volume data, or surface mesh data for the segments of the head. The lead geometry used in this study is the Medtronic 3389 DBS lead, the head model can be obtained from STL files. The head segments were necessary for volumetric mesh generation as the lead has to be incorporated into the head mesh. The required STL files were obtained from SimNIBS as discussed in section 4.2.2. The output from the headreco consisted of masks and STL files and part of their output. These STL files were used to generate a head mesh in MATLAB. The data needed for the lead was obtained from Lead-DBS as mentioned in section 4.2.1. The lead geometry used for this study is the Medtronic 3389 DBS lead and the orientation of the lead is according to the postoperative data obtained from a patient with PD. The surface data of the lead was extracted and the same data of the lead was used with the data from SimNIBS to generate the head mesh.

6.2 Mesh Generation

The mesh generation was performed using Iso2Mesh. Before generating the mesh, the files had to be brought into the same coordinate space as the STL files obtained from SimNIBS and the lead data obtained from Lead-DBS. This was necessary to superimpose the STL files of the head segments and achieve accurate placement of the lead within the head model. The output from SimNIBS is always in the world coordinate space and the lead data from Lead-DBS was based on the MNI2009b template. The STL files from SimNIBS and Lead-DBS were transformed to the coordinate space of MNI152NLin2009bAsym. This was done using the transformation matrix obtained from MNI152NLin2009bAsym within Lead-DBS. For mesh generation, the contact regions of the lead were taken rather than the whole lead as they are the source for simulations directly influencing the electric field and its effect. Including the entire lead, especially the insulation, significantly increases the complexity of the mesh. By simplifying the model only to include active contacts, simulations become more efficient without compromising the quality of the results. The Iso2Mesh function 'surf2mesh' was used to generate the volumetric mesh for the head model from STL files. The generated mesh file had to be converted to an XML file for use with FEMfuns. However, the output of Iso2mesh cannot be directly converted to an XML file using dolfin-convert, a conversion tool provided by the FEniCS toolbox. This tool requires the input mesh file to be in ASCII (American Standard Code for Information Interchange) format. To convert the mesh, the output from the mesh generation that was in double-precision floating point numbers were written in int32 format. Fieldtrip, a MATLAB toolbox, includes specialized functions to handle mesh files formatted in int32. This was used to write the mesh files in ASCII format, which can be used as input to the dolfin-convert function which creates the XML files as required by FEMfuns. Figure 4 shows the cross-section of the head model after merging the STL files of the head segments and contacts. Figure 5 shows the cross-section of the volumetric mesh generated for the same. Different regions of the head are shown in different colors. Figure 23 in the appendix A shows the contacts inside the mesh in space.

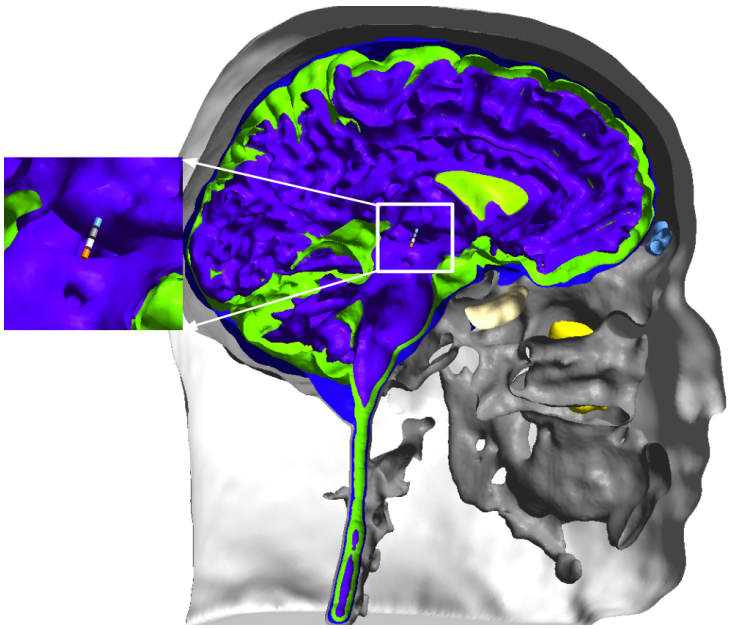

Figure 4: Cross section of the surface mesh created by merging the STL files of the head segments obtained from SimNIBS and the STL files of the contacts obtained from Lead-DBS. Different colors of the image show different parts of the head. The white box within the image highlights the placement of the lead. The contacts shown in the cross-section are the contacts placed on the left hemisphere of the brain. The enlarged image of the white box is given on the left side of the image.

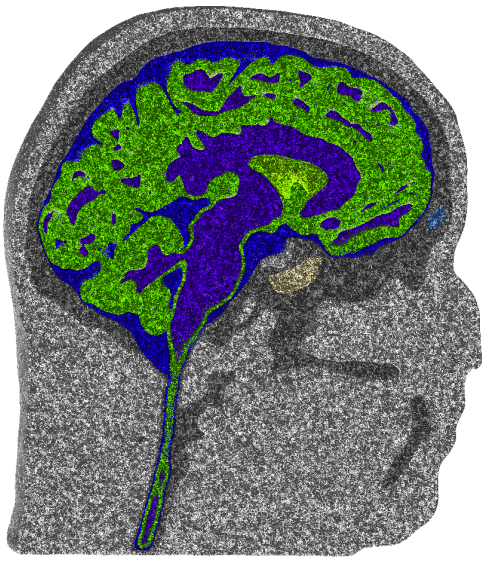

Figure 5: Cross section of the volumetric mesh generated from the STL files of the head segments obtained from SimNIBS and the STL files of the contacts obtained from Lead-DBS. Different colors of the image show different parts of the head. The image shows the same cross-section of the mesh as shown in figure 4. The visibility of the contacts is constrained for this cross-section.

6.3 Simulations in FEMfuns

This section will discuss the input parameters, the changes made to the initial solvers, and the various simulations performed using FEMfuns.

6.3.1 Input Parameters

The function dolfin-convert is used to convert the generated mesh to XML files of the mesh, its physical regions, and facet regions. The physical region refers to physical groups or tags applied to different domains of the mesh that can be used to identify different regions. The facet regions refer to the faces of the 3D data. It is used to identify the boundaries within the mesh. The input parameters of the FEMfuns are done by manually assigning the XML files of the outputs from the dolfin-convert command. When assigning the input parameters, the material of the regions had to be specified which has the options of resistive, conductive, and dispersive material. For this study, resistive condition was used. Then for the regions within the mesh, the volume markers for each region and its conductivities were assigned. The value of conductivities used for simulations and the volume markers used for the simulations are given in table 9 in the appendix. The conductivites of the head regions used for the simulation were taken from SimNIBs [41],[4]. The last parameter to specify is the current to be applied to the contacts. They are assigned as a points where the cathode and the anode are assigned. For this study, the current used was 2 milliAmperes (mA). For monopolar simulations, the cathode was assigned 2 mA and each anode was assigned -1 mA. For bipolar simulations, each cathodes were assigned 1 mA and each of the anodes was assigned -1 mA.

6.3.2 Changes in Solver

FEMfuns uses a Krylov solver for discretized linear equations. Initially, it tries to get the solution using CG solver type with a preconditioner ILU for 500 iterations. If the solver does not converge, it uses GMRES with precondition ILU with relative and absolute tolerance of 1e-1 which results in lower accuracy. This does not work for complex problems. The mesh used in this study is complex, as lead contacts are incorporated into it. The initial solvers of FEMfuns were able to find the solution for monopolar simulation but not for bipolar. The solver used was GMRES with the AMG preconditioner, which can be used for complex models. The tolerance was kept at 1e-9, which can result in higher precision. If the solver fails to find solutions, the fallback solver was also gmres with preconditioner amg but with a lower tolerance of 1e-6 which can result in lower accuracy. Figure 6 shows the numbering of contacts that will be used to refer to simulations. The two types of simulation used are monopolar and bipolar simulation. The centroids of each contact are used to assign the source and sink points for all simulations. Table 10 shows the centroids obtained for each contact.

6.3.3 Monopolar Simulations

For monopolar simulations, the source is placed in the neck region, since the neck is the furthest region in the mesh. The coordinates of the source location are -5.27,-27.72,-125.91 mm. Four simulations were done with monopolar configuration. Table 1 shows the anode position used for each simulation.

Simulations	Anode
1	contacts 16 and 20
2	contacts 17 and 21
3	contacts 18 and 22
4	contacts 19 and 23

Table 1: Table of Simulations for monopolar configuration

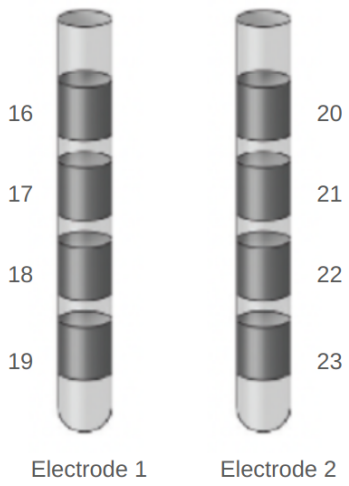

Figure 6: Contact on the left and right hemisphere of the brain are labeled according to the figure to specify the location of source and sink for different simulations

6.3.4 Bipolar Simulations

For bipolar simulations, one cathode and the anode at each lead are taken for each simulation. The cathode and the anode on each lead are taken by skipping one contact in between to have equal spacing between contacts for each simulation. Table 2 shows the configurations used for bipolar simulations.

Simulations	Cathode	Anode
1	contacts 16, 20	contacts 18, 22
2	contacts 17, 21	contacts 19, 23
3	contacts 18, 22	contacts 16, 20
4	contacts 19, 23	contacts 17, 21

Table 2: Table of Simulations for bipolar configuration

6.4 Additional Functions developed within FEMfuns

The following functions were developed to obtain the electric field and for the subsequent processing of these data.

1. **Generation of electric field**: The main objective of the study is to compare the electric field but FEMfuns by itself does not provide electric field data. FEMfuns only generated electric potential after running the simulations. Electric potentials are generated at the nodes of the cells. So an electric field had to be generated from the electric potential obtained from FEMfuns. The electric fields were calculated at the centroids of the cells. Centroids of the cells were preferred over nodes to get the electric field of the entire cell rather than the electric fields at the nodes of the cell. To obtain the electric field data, the **basis function** of FEniCS was used. FEniCS can evaluate functions at arbitrary points in a function space within the domain of a mesh which was used to find the electric fields at the centroids. Initially, it determines which element of the mesh contains that point of interest followed by transforming that point to the local coordinate system of the element. Then it uses the basis function defined on the element to compute the value at the given

points. For visualization, the electric field found at the centroids was projected onto a DG0 space using the **project** function. Projecting the electric field directly to a DG0 space can also get the gradient at the centroids, but projecting the gradient to CG1 and finding the electric field at the centroids was preferred to get the closest approximation at the centroids. This was done to keep the continuity of the gradient close to the gradient of the electric field initially generated from the potentials in CG1 function space.

2. **Electric field for specific subdomain**: The main objective of the study is to compare the electric field in the cortical regions of the brain. So getting the electric field at the grey matter would be sufficient to compare the electric field in cortical regions. To get the electric field from the mesh, the **submesh** function of FEniCS was used to create a submesh of grey matter. After creating the submesh, a vector function space specifying DG0 was created for the same. The electric field found at the centroids was projected onto the vector function space created for the submesh. This function can find the electric field for any subdomain when you specify the domain marker for that region. It also helps to reduce the computation time for a complex mesh as it only calculates it for the specified region rather than computing it for the whole mesh.

3. **Normal components of electric field**: To calculate the normal components of the electric field, the centroids of the subdomain were initially calculated. For the same submesh, the facet midpoints at the boundaries were calculated. For each midpoint of the cells in the submesh, the Euclidian distance to all the facet midpoints at the boundaries was calculated for all cells. For each cell, the index of the facet cell with minimum distance from the calculated distance was taken. For the facet obtained, the normal for the facet is found using the function **facet.normal()** in FEniCS, and each component of the normal was extracted to find the scale product of the electric field normal. With the electric field found at the centroids and the normals for the centroids, the electric field normals were calculated. The code was implemented in a sample unit square mesh divided into 10 X 10 grids of triangles. Figure 7 shows the direction of normals in red line for a few selected centroids for the sample mesh created. It shows that when computing normals, it takes the closest cell at the boundary for a given point.

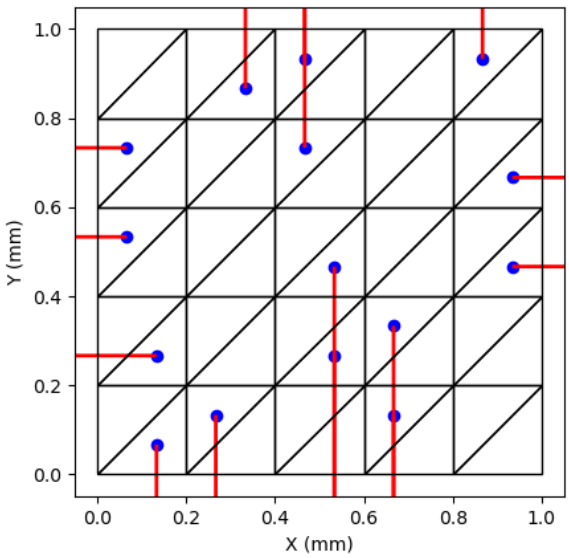

Figure 7: Visualization of the normal vectors at selected centroids of a finite element mesh within a unit square domain

With the newly incorporated functions in FEMfuns, the output now includes a CSV file containing data on the centroids, electric field components, the norm of the electric field, and the normal components of the electric field for the specified subdomain. Additionally, FEMfuns generates ParaView files that visualize the electric fields, normal components of the electric field, and the current density at the centroids of the entire head mesh and the specified subdomain.

6.5 Extracting Cortical Parcellations and Mapping Corresponding Electric Fields

The main objective of the study is to compare the electric field strengths in the cortical regions, so the parcellation of the brain is necessary to get the electric fields for each region. FreeSurfer was used to get the cortical parcellations of the brain. The T1-weighted MR image of the Ernie dataset was used to get the parcellation of the data from FreeSurfer. Figure 24 in the appendix shows the cortical parcellation of the Ernie data set. For this study, the Desikan-Killiany atlas was used because it has a smaller number of parcellations per hemisphere. Some regions needed for comparison were not found in the parcellated data, so label files generated by FreeSurfer were merged to obtain those regions. When using parcellated data from other atlases with more parcellations, the output after merging did not have the complete region or small parts of the whole region were missing compared to the Desikan-Killiany atlas. FreeSurfer has the orig.mgz file, which has the transformation to convert the parcellated files from the parcellated atlas space to the original space of the input T1-weighted MR image, so before using the parcellated data to obtain separate regions, the parcellated data were registered with the orig.mgz file to get the parcellated data in the initial space. Appendix B, Figure 25 shows the parcellated data with the gray matter of the file used to generate the mesh. After finding the labels or the regions to be merged, **mri_mergelabels** function was used to merge the label files for the left and right hemispheres. For regions for which the parcellated data were available as labels, **mri_binarize** function was used to get the .mgz files of the regions. Mgz files contain the volumetric data of the region which was used to get the STL files of the region using Iso2mesh. The STL files obtained were for each hemisphere, so after getting the regions for each hemisphere, the STL files of the left and right hemisphere data were merged for each region.

The parcellated data obtained from the Desikan-Killiany atlas was not in the same initial space as Ernie, so it was necessary to bring the STL files of the parcellated data in the same space as Ernie. From figure 26a, it can be seen that they are not aligned. To obtain the STL files in the same coordinate space as Ernie, the iterative Closest Point (ICP) algorithm for the point cloud was used. It is an algorithm used to align two-point clouds commonly used for registration and reconstruction [45]. It aims to minimize the difference between the two point clouds by iteratively refining the transformation (rotation and translation) that aligns one point cloud (source) to another (target). MATLAB has a function called **pcregistericp** which has to be provided with the point cloud for transformation and target point cloud. In this case, the point cloud for transformation was the STL files of the parcellated data, and the target files were the STL files of the cortical region from the head mesh used for the simulation. Figure 26b in section B shows the regions after using pcregistericp in the same space. The alignment of the STL files was verified by cross-referencing the coordinates of the centroids from the parcellation STL files with the centroids of the head mesh.

After the parcellated data was aligned, STL files were used to identify the centroids of tetrahedral elements within the head mesh that correspond to these regions. The MATLAB function **inpolyhedron** was used to determine which centroids fall inside the STL-defined regions. The function takes the STL files and a list of points as input and outputs the centroids located

within the STL boundaries. The electric field data at the centroids were post-processed.

6.6 Post processing Data

The 3D visualization of the data obtained was performed using ParaView and 3D Slicer. ParaView was utilized to visualize the electric potential, electric field, and current density obtained from FEMfuns. The electric fields obtained from the cortical parcellation were analyzed by calculating the mean magnitude, the maximum magnitude, and the normal components of the electric field in the centroids of the cells. The mean magnitude of the electric field was used to compare the electric fields across regions, accounting for non-uniform distribution. Regions near the stimulation site exhibit higher electric field magnitudes, while those farther away have lower magnitudes. To rule out this difference, the mean magnitude of the electric field is taken. This gives the average value of the electric field in the region as most of the cells in the region will have an electric field close to the average value of the electric field. The mean electric field values for the head model were used to color code the cortical parcellation, which was subsequently visualized using 3D Slicer. The parcellation file from FreeSurfer was initially relabeled to merge the left and right hemisphere regions. The relabeling was done such that, a specific region in the left and right hemispheres will have the same label. To map the regions to their simulation values, for all regions, the corresponding simulation value was assigned to each voxel in the segmentation data. To remove all the regions which were not included in the study such as CSF or ventricles were assigned to NaN (Not a Number) values to exclude from visualization.

The maximum value of the electric field within the regions is taken to understand the peak simulation levels for all simulations. To obtain the maximum value of the electric field, the 99.9th percentile of the data is taken. Taking the 99.9th percentile of data is essential for effectively managing outliers, which can arise from simulation noise and can distort results. By excluding the top 0.1 percent of these extreme values, the analysis yields a more accurate and consistent representation of the data. The normal components of the electric field were obtained by multiplying the electric field by its normal vector for each region.

Once the data for cortical parcellations were obtained, certain regions were selected for further comparison because they are involved in the Cortico-Basal Ganglia-thalamocortical loop. The regions included the Auditory cortex, Brainstem, Caudate, Cerebellar cortex, Inferior parietal cortex, Insula, Postcentral gyrus, Precentral gyrus, Prefrontal cortex, Premotor cortex, Postral anterior cingulate cortex, Superior parietal cortex, Thalamus, and Visual cortex. Focusing the analysis on these specific regions enables a more detailed comparison, and this approach makes analysis more manageable for more precise analysis and visualization. Histograms were then used to visualize the electric field distribution within these regions as it provided a clear and intuitive way to see how electric field values are distributed across the region for different simulations. They show the frequency of data points within specified ranges (bins), making it easy to identify patterns. It helps to display the range of electric fields across the region and allows for comparison of the shape and spread of electric fields.

7 Results

As discussed in section 6.3, the monopolar and bipolar simulations were carried out. The electric potential and electric field data for each simulation were obtained and post-processed.

7.1 3-D Visualization of the Results

Initially, the results obtained from the simulations were visually inspected using ParaView software. Figures 8 and 9 illustrate the results of monopolar and bipolar stimulation configurations, respectively.

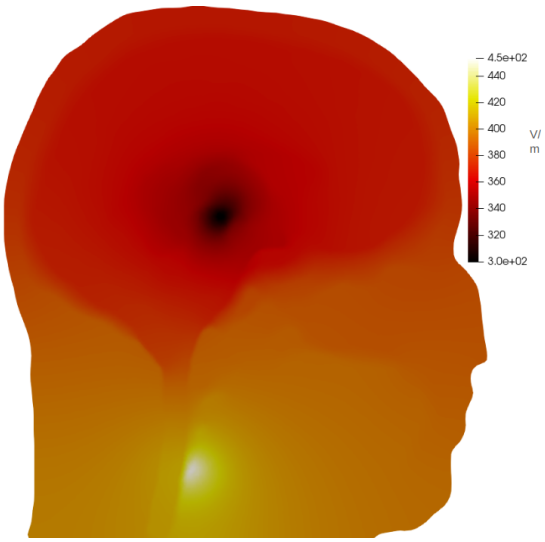

(a) Electric Potential generated in FEMfuns

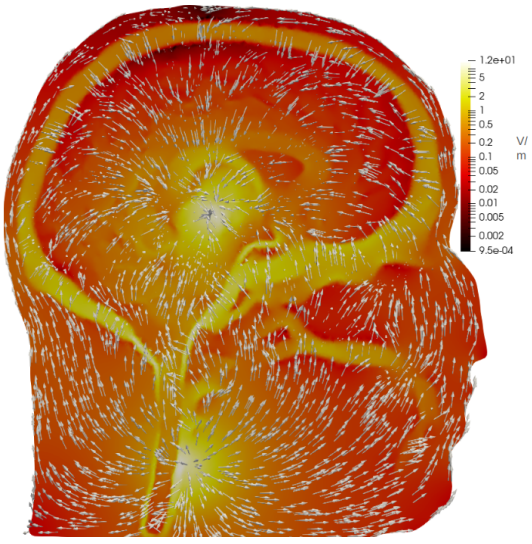

(b) Magnitude of Electric Field

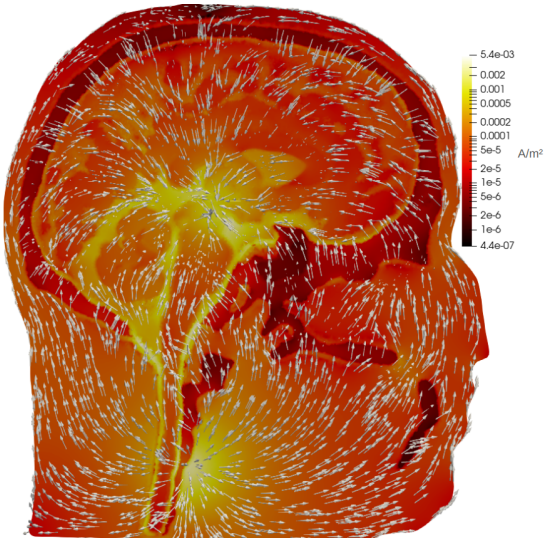

(c) Current Density

Figure 8: Figure shows the electric potential, electric field, and current density for a cross-section of the head model for monopolar configuration. Arrows in figure 8b and 8c indicate the direction of flow of electric field and current density respectively

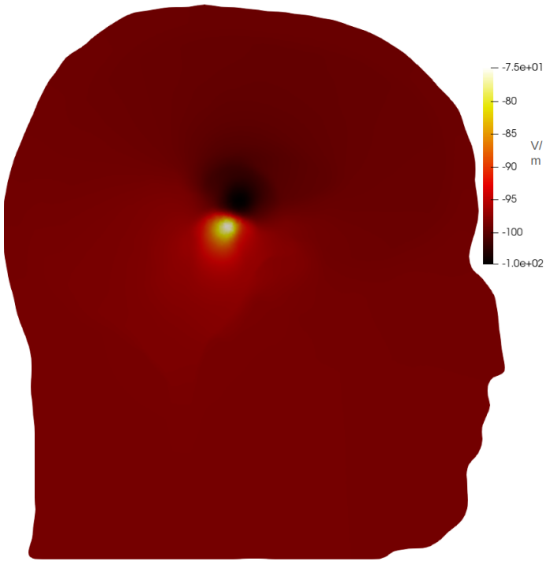

(a) Electric Potential generated in FEMfuns

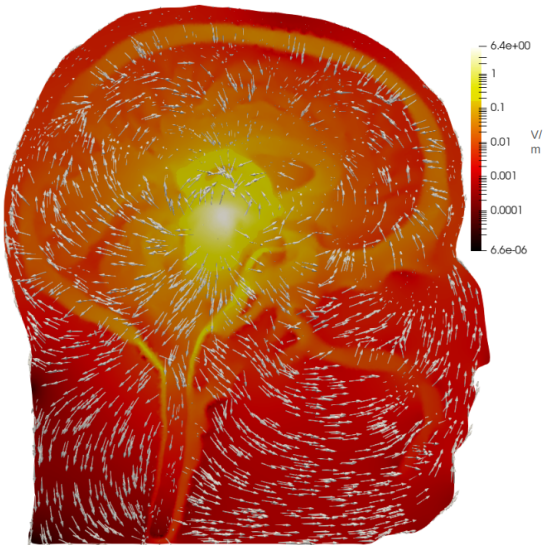

(b) Magnitude of Electric Field

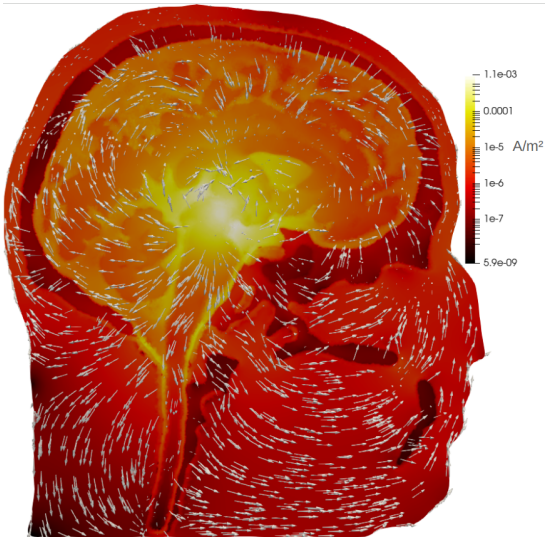

(c) Current Density

Figure 9: Figure shows the electric potential, electric field, and current density for a cross-section of the head model for bipolar configuration. Arrows in the figure 9b and 9c indicates the direction of flow of electric field and current density respectively

These figures provide a comprehensive visualization of the electric potential, electric field, and current density distributions in the head model. The electric potential distribution reveals a gradient with the highest positive values near the neck region where the source is given and the highest negative values near the contacts. The electric field distribution highlights areas of high field strength concentrated near the point of positive change in the neck region and the contacts, with the field lines starting from the neck region and moving towards the electrode is shown in figure 8b. The current density follows a similar pattern to the electric field, with the highest density near the electrode contact, indicating a strong flow of electric current in these regions which is shown in figure 9c. Figure 9 illustrates the results of the bipolar configuration, showing the distribution of the electric potential, electric field, and current density. The potential distribution and current density in the bipolar configuration are more concentrated between the

source and the sink, creating a localized field as shown in figures 9b and 9c. Figure 27a and 27b in the appendix shows the coronal cross-section of the head model for monopolar and bipolar simulations respectively.

7.2 Analysis of Magnitude of Electric Field and Normal Components of Electric Fields in Cortical Parcellations

The electric field data for the cortical parcellations were derived from the results obtained using FEMfuns. For each of the 49 regions in the parcellated data, the mean magnitude, maximum values, and normal components of the electric field were calculated. These detailed results are provided in Appendix E. In this section, however, we present only the data for the focused region to facilitate better analysis. Table 12 in appendix shows the mean magnitude for the electric field for the cortical parcellations, and figure 28 shows the bar graph for the same.

Table 3: Table shows the Mean Magnitude of Electric Field Values for Selected Regions in Monopolar and Bipolar simulations

Region	**Bipolar Simulations(V/m)**				**Monopolar (V/m)**			
	Simulation 1	**Simulation 2**	**Simulation 3**	**Simulation 4**	**Simulation 1**	**Simulation 2**	**Simulation 3**	**Simulation 4**
Auditory Cortex	0.0022	0.0024	0.0022	0.0024	0.0154	0.0160	0.0166	0.0173
Brainstem	0.0318	0.0299	0.0318	0.0299	0.0871	0.0841	0.0814	0.0794
Caudate	0.0387	0.0353	0.0388	0.0353	0.1192	0.1136	0.1083	0.1036
Cerebellar Cortex	0.0765	0.0745	0.0765	0.0745	0.1807	0.1776	0.1747	0.1709
Inferior Parietal Cortex	0.0760	0.0784	0.0760	0.0784	0.1748	0.1804	0.1858	0.1896
Insula	0.0427	0.0416	0.0427	0.0416	0.1199	0.1194	0.1185	0.1165
Postcentral Gyrus	0.0455	0.0463	0.0455	0.0463	0.1149	0.1159	0.1169	0.1172
Precentral Gyrus	0.0969	0.1099	0.0969	0.1099	0.1786	0.2063	0.2350	0.2556
Prefrontal Cortex	0.0088	0.0085	0.0088	0.0085	0.0373	0.0370	0.0367	0.0367
Premotor Cortex	0.0052	0.0055	0.0052	0.0055	0.0278	0.0284	0.0291	0.0297
Rostral Anterior Cingulate Cortex	0.0321	0.0329	0.0321	0.0329	0.0951	0.0955	0.0963	0.0972
Superior Parietal Cortex	0.0800	0.0790	0.0800	0.0790	0.1813	0.1792	0.1779	0.1756
Thalamus	0.0499	0.0515	0.0499	0.0515	0.1299	0.1412	0.1497	0.1543
Visual Cortex	0.0156	0.0150	0.0156	0.0150	0.0532	0.0522	0.0514	0.0509

Table 4: Table shows the Magnitude of the maximum value of the electric field for the selected regions for monopolar and bipolar simulations

Region	**Bipolar Simulations(V/m)**				**Monopolar (V/m)**			
	Simulation 1	**Simulation 2**	**Simulation 3**	**Simulation 4**	**Simulation 1**	**Simulation 2**	**Simulation 3**	**Simulation 4**
Auditory Cortex	0.0364	0.0381	0.0363	0.0381	0.2237	0.2226	0.2214	0.2201
Brainstem	3.3588	2.5490	3.3588	2.5490	4.7692	3.0641	2.8175	3.5041
Caudate	2.7944	2.2625	2.7944	2.2625	3.9108	2.9724	3.1065	3.3456
Cerebellar Cortex	2.7944	2.3835	2.7944	2.3835	3.9108	2.7114	3.1065	3.5102
Inferior Parietal Cortex	2.4543	2.5490	2.4543	2.5490	3.6733	2.7114	3.1065	3.5102
Insula	1.8970	2.3887	1.8970	2.3887	1.9600	2.4314	3.1065	3.5102
Postcentral Gyrus	2.3181	2.5490	2.3181	2.5490	3.3349	2.5375	2.8857	3.5102
Precentral Gyrus	1.8970	2.3598	1.8970	2.3598	1.6545	2.2228	3.1065	3.3523
Prefrontal Cortex	3.8006	2.5490	3.8006	2.5490	5.2999	3.0641	2.5425	3.5102
Premotor Cortex	0.5638	0.4388	0.5638	0.4388	0.8669	0.9631	0.9553	0.8331
Rostral Anterior Cingulate Cortex	1.8970	2.5490	1.8970	2.5490	2.6289	2.7114	3.1065	3.5102
Superior Parietal Cortex	1.8970	2.4123	1.8970	2.4123	2.4906	2.4407	3.1065	3.5102
Thalamus	0.8410	0.8515	0.8410	0.8515	1.3965	1.5964	1.6434	1.5519
Visual Cortex	3.8006	2.3598	3.8006	2.3598	5.2999	3.0641	3.1065	3.5102

Table 13 in the appendix shows the maximum value of the electric field for each region and figure 29 shows the bar graph. Since the electric fields are calculated at the centroids of the cells, there might be simulation noise that can possibly make outliers. To address this, the 99.9th percentile of the data is considered, effectively removing the top 0.1 percent of the data, which are likely outliers. This approach provides a more accurate representation of the simulation results by mitigating the effect of noise in the data. Table 14 in the appendix shows the maximum electric field within the regions after taking the 99.9th percentile of the electric field data and figure 30 shows the bar chart for the same.

Table 5: Table shows the Magnitude of the maximum value of the electric field for the selected regions for monopolar and bipolar configurations taking 99.9th percentile of the data

Region	**Bipolar Simulations(V/m)**				**Monopolar (V/m)**			
	Simulation 1	**Simulation 2**	**Simulation 3**	**Simulation 4**	**Simulation 1**	**Simulation 2**	**Simulation 3**	**Simulation 4**
Auditory Cortex	0.0223	0.0244	0.0223	0.0244	0.1019	0.1031	0.1035	0.1042
Brainstem	1.4111	1.2300	1.4111	1.2300	2.2051	1.8134	1.4827	1.3996
Caudate	1.4633	1.1285	1.4633	1.1285	2.2695	1.7842	1.5220	1.2766
Cerebellar Cortex	1.6173	1.4349	1.6173	1.4349	2.2170	1.9097	2.2068	2.3040
Inferior Parietal Cortex	1.4327	1.7747	1.4327	1.7747	1.7607	1.9824	2.2060	2.6902
Insula	1.0083	1.0935	1.0083	1.0935	1.2865	1.3993	1.7253	1.7824
Postcentral Gyrus	1.1870	1.2846	1.1870	1.2846	1.5208	1.5990	1.8798	2.0028
Precentral Gyrus	1.5640	1.9373	1.5640	1.9373	1.3354	1.8766	2.5127	2.9576
Prefrontal Cortex	0.4986	0.4740	0.4986	0.4740	0.9142	0.7901	0.6996	0.6459
Premotor Cortex	0.1842	0.1847	0.1842	0.1847	0.4920	0.4649	0.4171	0.3676
Rostral Anterior Cingulate Cortex	1.0614	1.3083	1.0614	1.3083	1.3026	1.3937	1.7723	2.1285
Superior Parietal Cortex	1.3439	1.6395	1.3439	1.6395	1.5456	1.6795	2.1537	2.5983
Thalamus	0.5103	0.6272	0.5103	0.6272	1.1197	1.2577	1.1695	1.0219
Visual Cortex	1.0096	0.9163	1.0096	0.9163	1.5557	1.3526	1.1627	1.0998

Table 6: Table shows the mean of the normal components of electric field for the selected regions for monopolar and bipolar simulations

Region	**Bipolar Simulations(V/m)**				**Monopolar (V/m)**			
	Simulation 1	**Simulation 2**	**Simulation 3**	**Simulation 4**	**Simulation 1**	**Simulation 2**	**Simulation 3**	**Simulation 4**
Auditory Cortex	0.0015	0.0016	0.0014	0.0015	0.0096	0.0100	0.0104	0.0108
Brainstem	0.0193	0.0177	0.0203	0.0187	0.0579	0.0555	0.0527	0.0506
Caudate	0.0233	0.0205	0.0248	0.0226	0.0805	0.0763	0.0718	0.0676
Cerebellar Cortex	0.0417	0.0398	0.0465	0.0432	0.1204	0.1156	0.1101	0.1048
Inferior Parietal Cortex	0.0385	0.0374	0.0464	0.0444	0.1109	0.1122	0.1114	0.1088
Insula	0.0249	0.0241	0.0254	0.0245	0.0793	0.0784	0.0769	0.0752
Postcentral Gyrus	0.0243	0.0243	0.0267	0.0255	0.0706	0.0701	0.0692	0.0679
Precentral Gyrus	0.0402	0.0452	0.0569	0.0619	0.1119	0.1216	0.1298	0.1340
Prefrontal Cortex	0.0056	0.0053	0.0057	0.0054	0.0247	0.0245	0.0243	0.0243
Premotor Cortex	0.0035	0.0036	0.0034	0.0035	0.0183	0.0188	0.0193	0.0198
Rostral Anterior Cingulate Cortex	0.0178	0.0176	0.0193	0.0188	0.0621	0.0614	0.0606	0.0599
Superior Parietal Cortex	0.0452	0.0438	0.0473	0.0450	0.1127	0.1083	0.1040	0.0996
Thalamus	0.0284	0.0306	0.0367	0.0374	0.0906	0.0951	0.0980	0.0993
Visual Cortex	0.0093	0.0088	0.0100	0.0093	0.0344	0.0336	0.0328	0.0322

Table 7: Table shows the mean magnitude of current density for the selected regions for monopolar and bipolar simulations

Region	**Bipolar Simulations (A/m^2)**				**Monopolar Simulations (A/m^2)**			
	Simulation 1	**Simulation 2**	**Simulation 3**	**Simulation 4**	**Simulation 1**	**Simulation 2**	**Simulation 3**	**Simulation 4**
Auditory Cortex	0.0006	0.0007	0.0006	0.0007	0.0043	0.0044	0.0046	0.0048
Brainstem	0.0088	0.0083	0.0088	0.0083	0.0240	0.0232	0.0225	0.0219
Caudate	0.0107	0.0097	0.0107	0.0097	0.0329	0.0314	0.0299	0.0286
Cerebellar Cortex	0.0211	0.0206	0.0211	0.0206	0.0499	0.0490	0.0482	0.0472
Inferior Parietal Cortex	0.0210	0.0216	0.0210	0.0216	0.0482	0.0498	0.0513	0.0523
Insula	0.0118	0.0115	0.0118	0.0115	0.0331	0.0330	0.0327	0.0322
Postcentral Gyrus	0.0126	0.0128	0.0126	0.0128	0.0317	0.0320	0.0323	0.0324
Precentral Gyrus	0.0267	0.0303	0.0267	0.0303	0.0493	0.0569	0.0649	0.0705
Prefrontal Cortex	0.0024	0.0023	0.0024	0.0023	0.0103	0.0102	0.0101	0.0101
Premotor Cortex	0.0014	0.0015	0.0014	0.0015	0.0077	0.0079	0.0080	0.0082
Thalamus	0.0138	0.0142	0.0138	0.0142	0.0359	0.0390	0.0413	0.0426
Visual Cortex	0.0043	0.0041	0.0043	0.0041	0.0147	0.0144	0.0142	0.0140

Additionally, the mean magnitude of the normal components of the electric field for each region is presented in table 15 with figure 31 that illustrates these data in a bar graph which was obtained by multiplying the electric field by its normal vector.

From the cortical parcellation regions, certain regions are particularly focused on due to their involvement in the thalamocortical loop. Table 3 presents the mean values of the magnitude of the electric field for selected regions in monopolar and bipolar simulations. The regions include the Auditory cortex, Brainstem, Caudate, Cerebellar cortex, cerebellar cortex, Insula, Post-central gyrus, Precentral gyrus, Prefrontal cortex, Premotor cortex, Anterior rostral cingulate cortex, Superior parietal cortex, Thalamus, and Visual cortex. The corresponding bar graph in Figure 10 highlights that monopolar configurations generally show higher mean electric field values compared to bipolar configurations in these regions.

Table 4 presents the magnitude of the maximum electric field values for the selected regions in monopolar and bipolar simulations. Figure 11 is a bar chart that visualizes these maximum electric field values across the different brain regions. Table 5 shows the magnitude of the maximum electric field for the selected regions after taking the 99.9th percentile of the data, which removes potential outliers and provides a more accurate representation of the simulation results. Figure 12 shows the bar graph to visualize the same. Table 6 presents the mean of the normal components of the electric field for the selected regions. Figure 13 shows the bar graph for the same. Table 7 shows the mean current density of the selected regions and figure 14 shows the bar chart for the same.

From table 3 and figure 10, it can be seen that the minimum magnitude of the electric field for monopolar simulations is 0.0154 V/m for monopolar simulation 1 and monopolar simulation 4 has the maximum magnitude of the electric field as 0.2556 V/m. For the mean magnitude of the electric field, monopolar simulation 1 has a minimum value of 0.0154 V/m and a maximum value of 0.1813 V/m. Monopolar simulation 2 has a minimum value of 0.016 V/m and a maximum value of 0.2053 V/m. Monopolar simulation 3 has a minimum value of 0.0166 V/m and a maximum value of 0.235 V/m. Monopolar simulation 4 has a minimum value of 0.0173 V/m and a maximum value of 0.2556 V/m. The minimum value for the mean magnitude of the electric field for bipolar simulation 1 is 0.0015 V/m and the maximum value is 0.0542 V/m. For bipolar simulation 2, the minimum value is 0.0016 V/m and the maximum value is 0.046 V/m. The minimum value for bipolar simulation 3 is 0.0014 V/m and the maximum value is 0.0509 V/m. For bipolar simulation 4, the minimum value is 0.0015 and the maximum value is 0.0444 V/m. So, the mean magnitude of the electric field ranges from 0.0014 V/m to 0.0542 V/m for bipolar simulations.

The maximum electric field strength observed in the monopolar configuration is notably higher compared to the bipolar configuration. Bipolar simulations show consistent values for the maximum values for electric field with a maximum value of 1.9373 V/m and while monopolar simulations have values above 1V/m for most of the regions. Some regions show a maximum value above 2 V/m except for monopolar simulation 2. In addition to the mean magnitude and maximum value of the electric fields, current density was also calculated for the focused regions. The current density for the selected regions was obtained by multiplying the mean magnitude of the electric field for the selected regions with the conductivity value ($J = \sigma E$) of GM which is 0.276 S/m. The current density obtained for the regions is given in table 7 and in figure 14. For Bipolar Simulation 1, the current density ranges from 0.0006 A/m^2 to 0.0267 A/m^2. In Bipolar Simulation 2, the range is from 0.0007 A/m^2 to 0.0283 A/m^2. Similarly, Bipolar Simulation 3 has a current density range of 0.0006 A/m^2 to 0.0267 A/m^2, and Bipolar Simulation 4 ranges from 0.0007 A/m^2 to 0.0283 A/m^2.

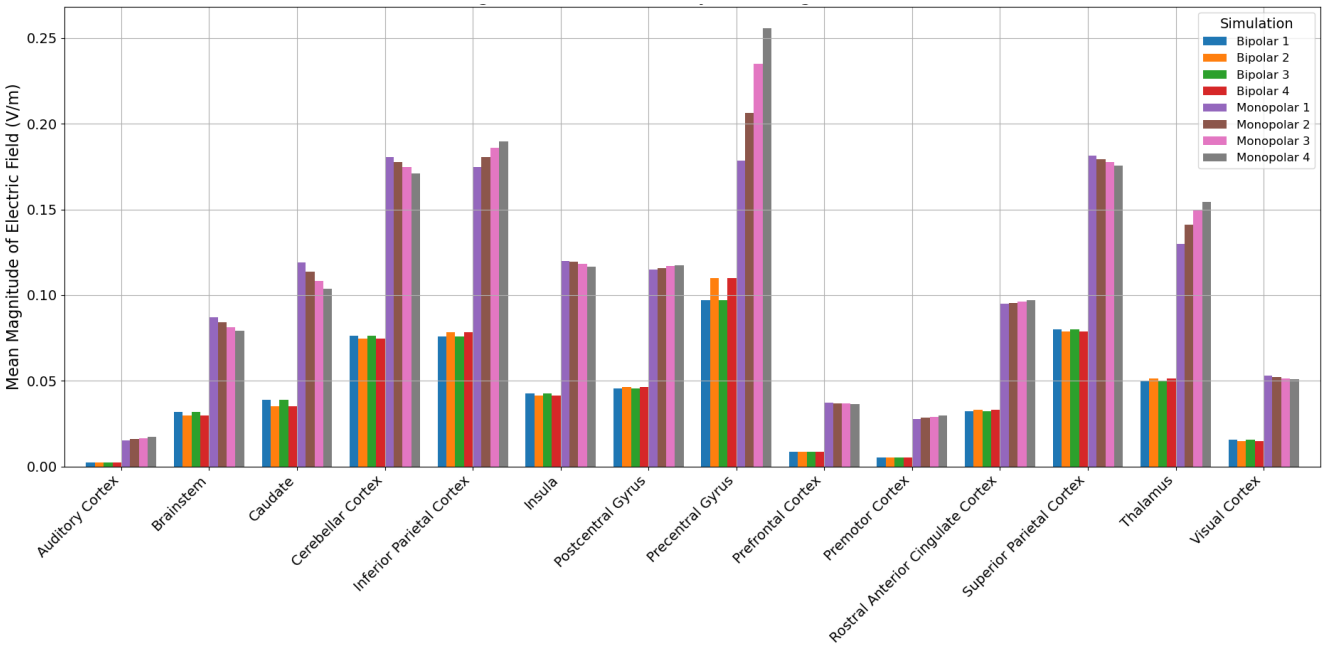

Figure 10: Bar graph shows the mean magnitude of electric field obtained from the selected region for monopolar and bipolar simulations

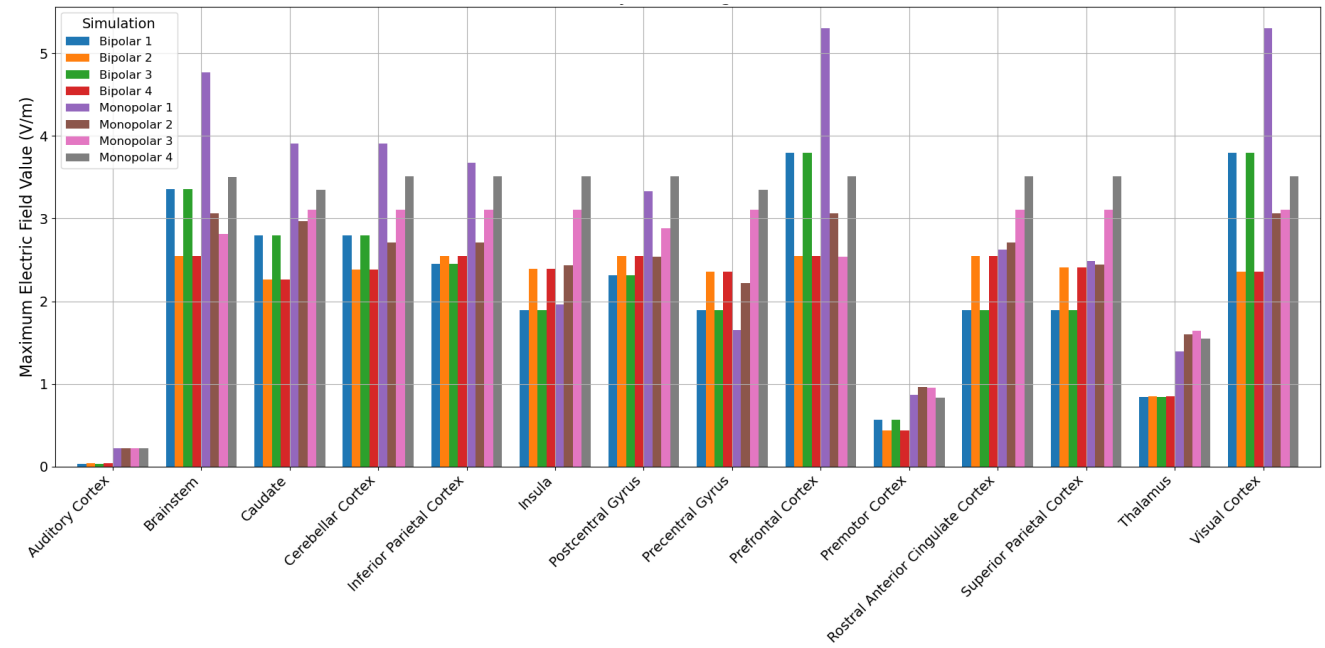

Figure 11: Bar graph showing the magnitude of maximum electric field for each simulation for the selected regions for monopolar and bipolar configurations

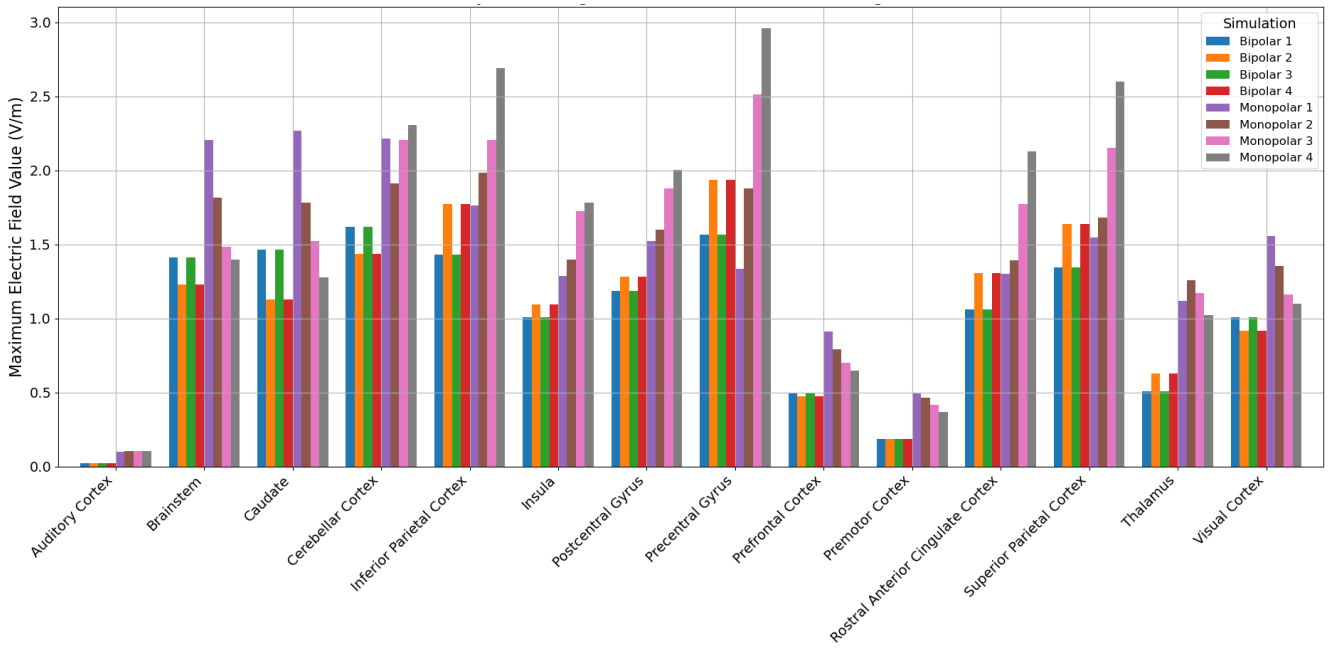

Figure 12: Bar graph showing the magnitude of maximum electric field for each simulation for selected regions after taking 99.9th percentile of the electric field for each region

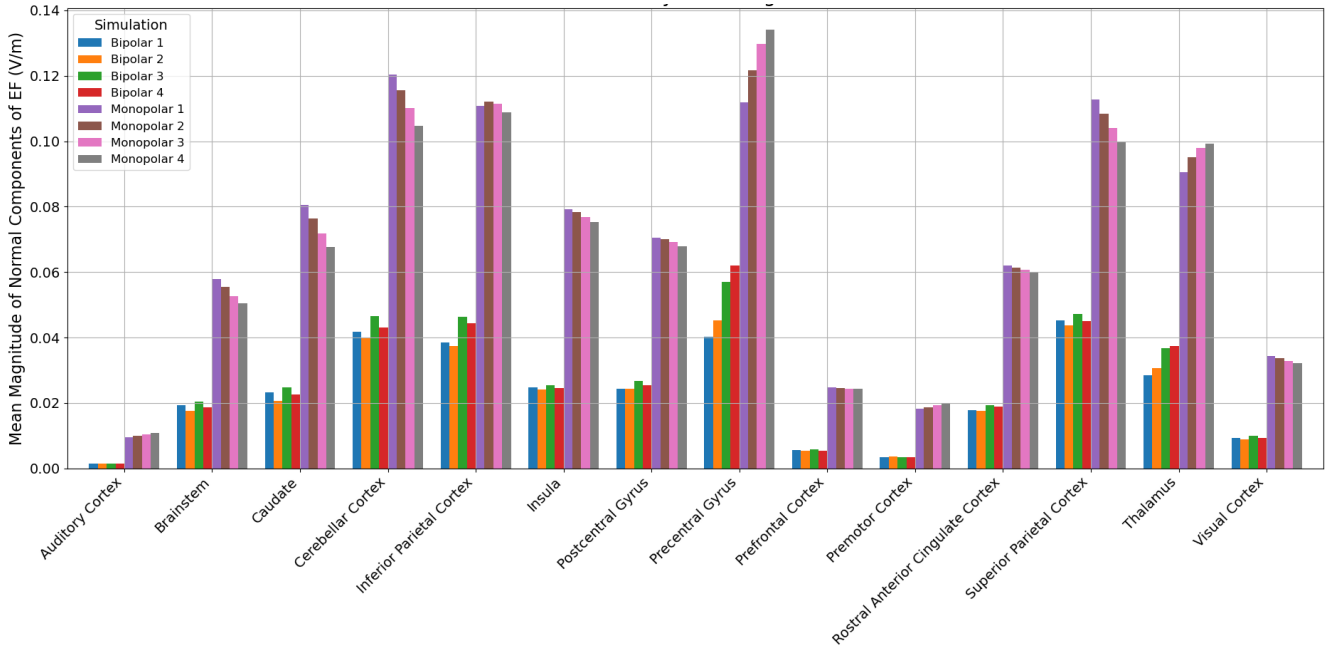

Figure 13: Bar graph showing the mean magnitude of the normal components of the electric field of each region for monopolar and bipolar simulation

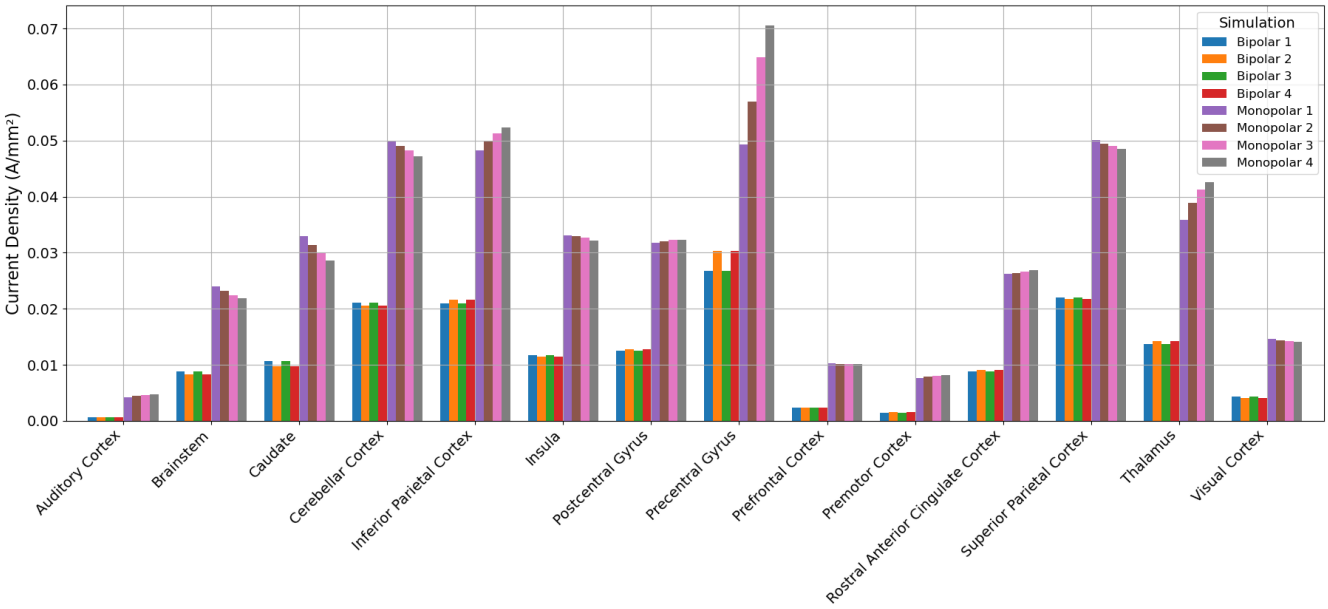

Figure 14: Bar graph shows the mean magnitude of current density obtained for the selected region for monopolar and bipolar simulations

For the Monopolar Simulations, the ranges are generally higher. Monopolar Simulation 1 shows a current density range from 0.0030 A/m^2 to 0.0492 A/m^2. Monopolar Simulation 2 has a range of 0.0043 A/m^2 to 0.0513 A/m^2. In Monopolar Simulation 3, the current density ranges from 0.0066 A/m^2 to 0.0659 A/m^2, while Monopolar Simulation 4 exhibits the highest range, from 0.0045 A/m^2 to 0.0705 A/m^2. The current density from monopolar simulations ranges from 0.0006 A/m^2 to 0.0283 A/m^2. For monopolar simulations, the current density ranges from 0.03 A/m^2 to 0.0705 A/m^2. Given the relevance of electric field studies in the literature and the need to address the research question on the electric field, the study is more focused on the electric field.

7.2.1 Analysis of the magnitude of weak electric fields

The analysis of the magnitude of weak electric fields is done by selecting some regions far from the electrode stimulation site. Caudate, Insula, Lingual cortex, Paracentral lobule, Parahip-

Table 8: Table shows the mean magnitude of electric field for the selected regions for monopolar and bipolar simulations

Region	Bipolar Simulations (V/m)				Monopolar Simulations (V/m)			
	Simulation 1	Simulation 2	Simulation 3	Simulation 4	Simulation 1	Simulation 2	Simulation 3	Simulation 4
Caudate	0.0387	0.0353	0.0387	0.0353	0.1193	0.1137	0.1083	0.1036
Insula	0.0427	0.0416	0.0427	0.0416	0.1199	0.1194	0.1185	0.1165
Lingual Cortex	0.0465	0.0466	0.0465	0.0466	0.1223	0.1270	0.1289	0.1268
Paracentral Lobule	0.0546	0.0562	0.0546	0.0562	0.1294	0.1396	0.1481	0.1526
Parahippocampal Cortex	0.0391	0.0410	0.0391	0.0410	0.1105	0.1204	0.1298	0.1374
Postcentral Gyrus	0.0455	0.0463	0.0455	0.0463	0.1149	0.1159	0.1169	0.1172
Thalamus	0.0499	0.0515	0.0499	0.0515	0.1299	0.1412	0.1497	0.1543

pocampal cortex, Postcentral gyrus, and Thalamus were the regions taken for this analysis. Within the simulations for regions away from the stimulation site, bipolar simulation 1 has the least mean magnitude of electric fields.

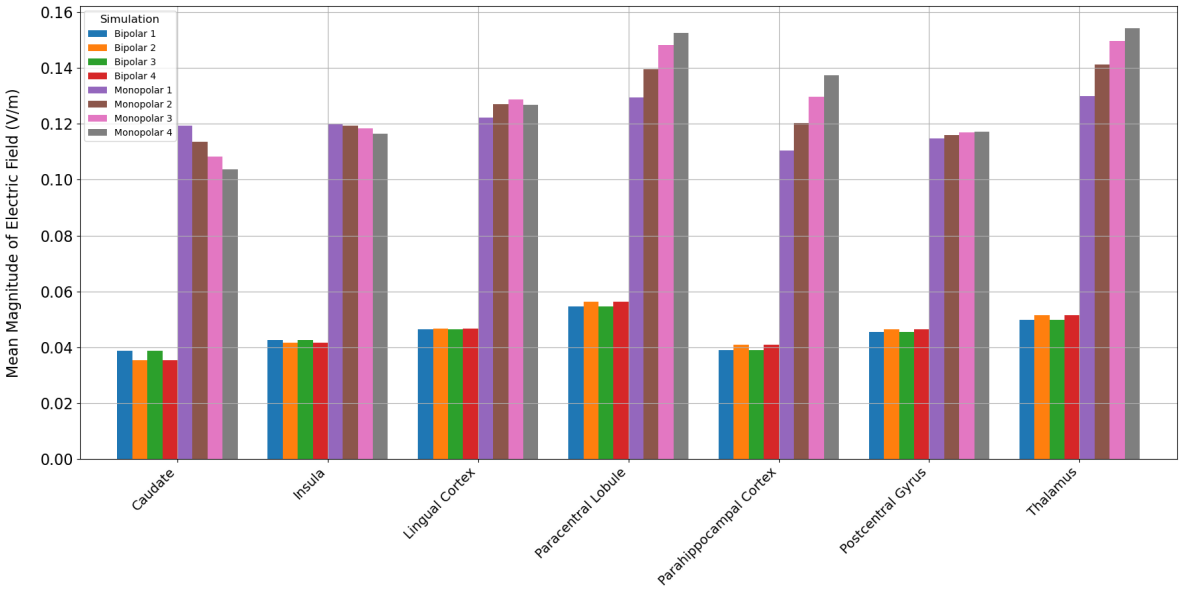

Figure 15: Bar graph showing the mean magnitude of the electric field of each region for monopolar and bipolar simulation for selected regions away from the simulation site

Bipolar simulation 1 ranges from 0.0387 V/m to 0.0546 V/m. The bipolar simulation ranges from 0.0353 V/m to 0.0562 V/m. Bipolar simulation 3 ranges from 0.0387 V/m to 0.0546 V/m, and bipolar simulation 4 ranges from 0.0353 V/m to 0.0562 V/m. For monopolar configurations, monopolar simulation 1 ranges from 0.1105 V/m to 0.1299 V/m. Monopolar simulation 2 ranges from 0.1137 V/m to 0.1412 V/m. Monopolar simulation 3 ranged from 0.1083 V/m to 0.1497 V/m, and monopolar simulation 4 ranged from 0.1036 V/m to 0.1543 V/m.

7.2.2 Color Coding Cortical Parcellation based on the mean magnitude of electric field

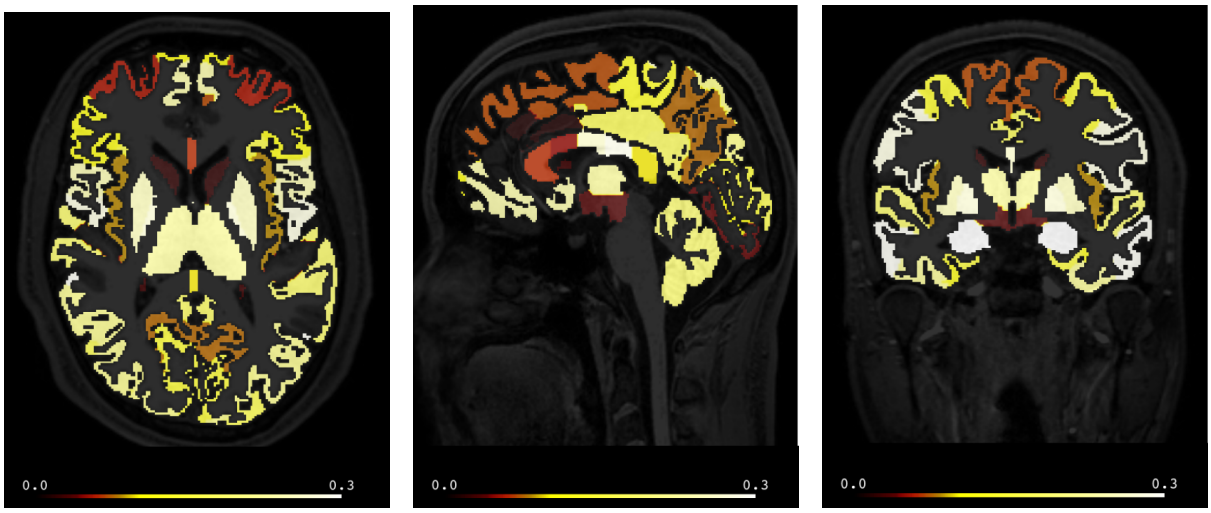

(a) Axial View (b) Sagittal View (c) Coronal View

Figure 16: Color-coded parcellation views based on the mean magnitude of electric field for monopolar simulation 4 with (a) Axial, (b) Sagittal, and (c) Coronal cross-section. The color bar at the bottom of the figure represents the mean magnitude of the electric field from 0 to 0.3 V/m

The mean magnitude electric field data obtained for the cortical parcellations were used to color-code the parcellation file obtained from FreeSurfer. The mean magnitudes of monopolar simulation 4 and bipolar simulation 4 were used to color code the cortical parcellations as shown in figure 16 and 17 respectively. It can be seen from figure 17 that bipolar simulations are more localized compared to monopolar simulation in figure 16.

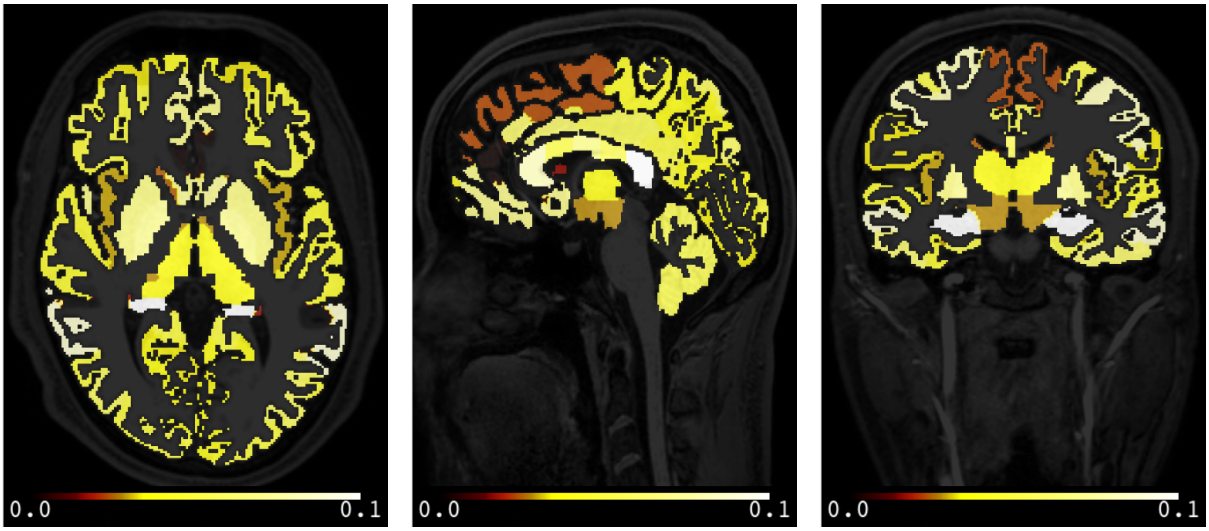

(a) Axial View (b) Sagittal View (c) Coronal View

Figure 17: Color-coded parcellation views based on the mean magnitude of electric field for bipolar simulation 4 with (a) Axial, (b) Sagittal, and (c) Coronal cross-section. The color bar at the bottom of the figure represents the mean magnitude of the electric field from 0 to 0.1 V/m

7.3 In-depth analysis of Premotor Cortex and Precentral Gyrus

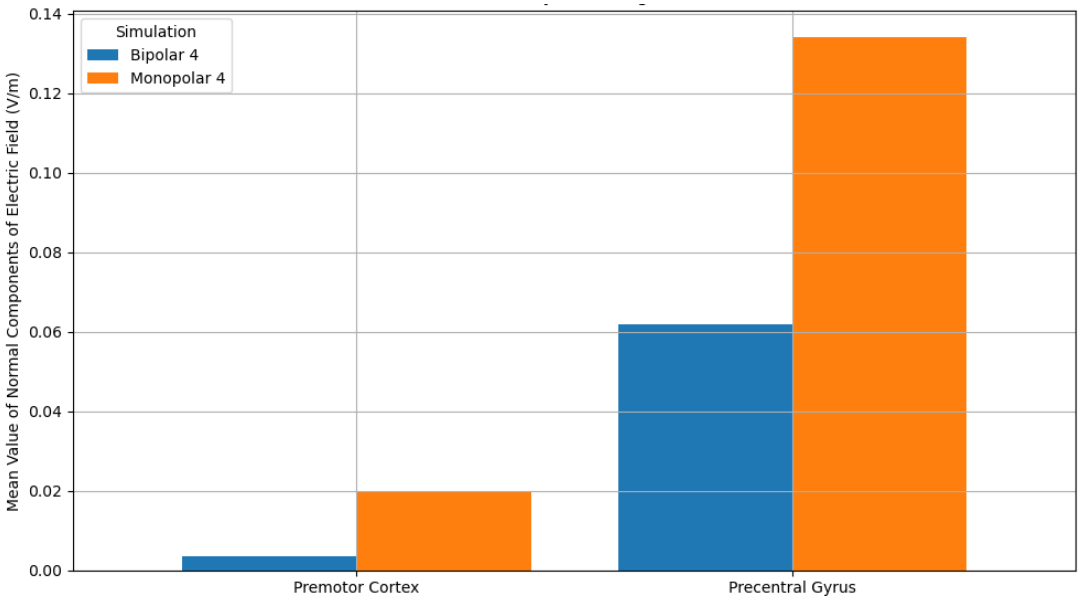

Figure 18: Comparison of the mean magnitude of the normal components of electric field for Precentral gyrus and Premotor cortex for monopolar and bipolar simulation 4

To further compare the simulations, monopolar simulation 4 and bipolar simulation 4 were taken as both have the highest magnitude of electric field for most of the regions. For a better comparison of the results, the Premotor cortex and Precentral gyrus were selected.

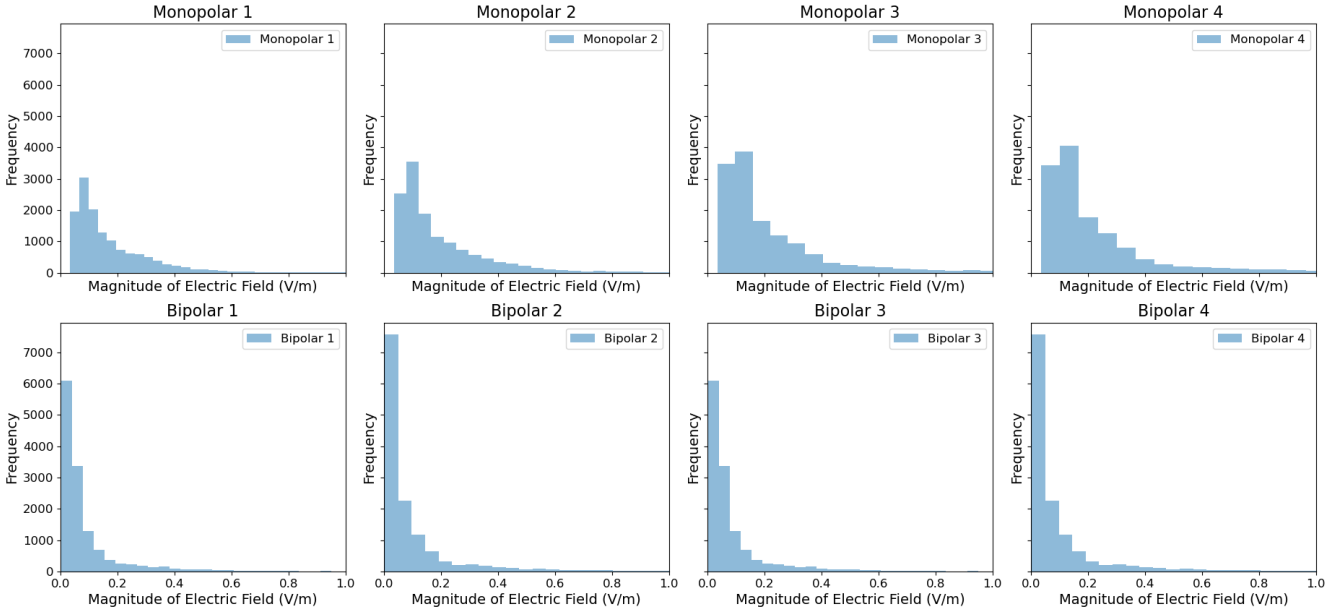

Figure 19: Histogram for the visualization of the magnitude of electric field distribution for Precentral gyrus for all simulations with the frequency of occurrence on the y-axis and the magnitude of electric field on the x-axis

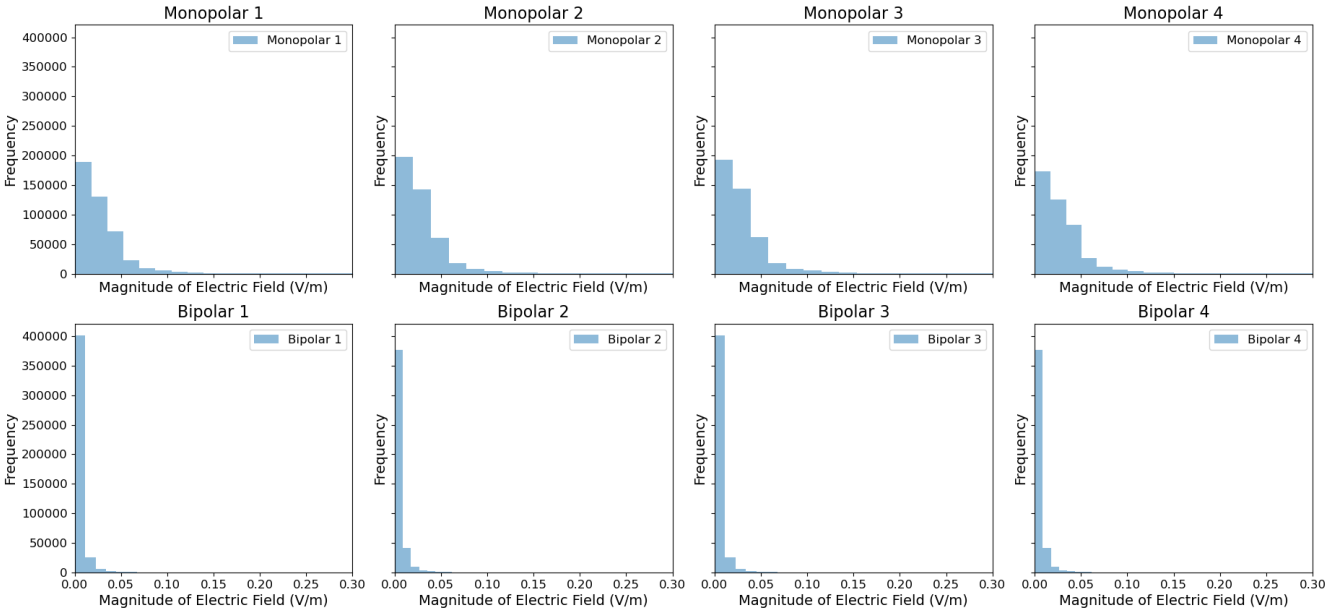

Figure 20: Histogram for the visualization of the magnitude of electric field distribution for Premotor cortex for all simulations with the frequency of occurrence on the y-axis and the magnitude of electric field on the x-axis

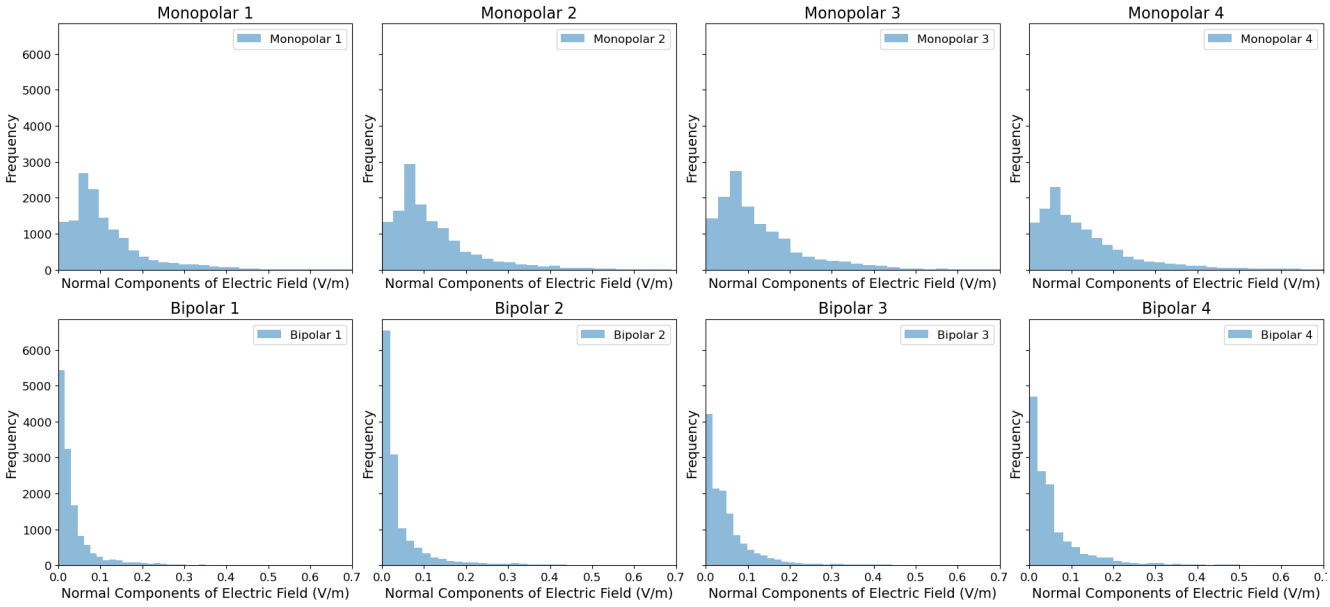

Figure 21: Histogram for the visualization of the distribution of the normal components of electric field for Precentral gyrus for all simulations with the frequency of occurrence on the y-axis and the magnitude of electric field on the x-axis

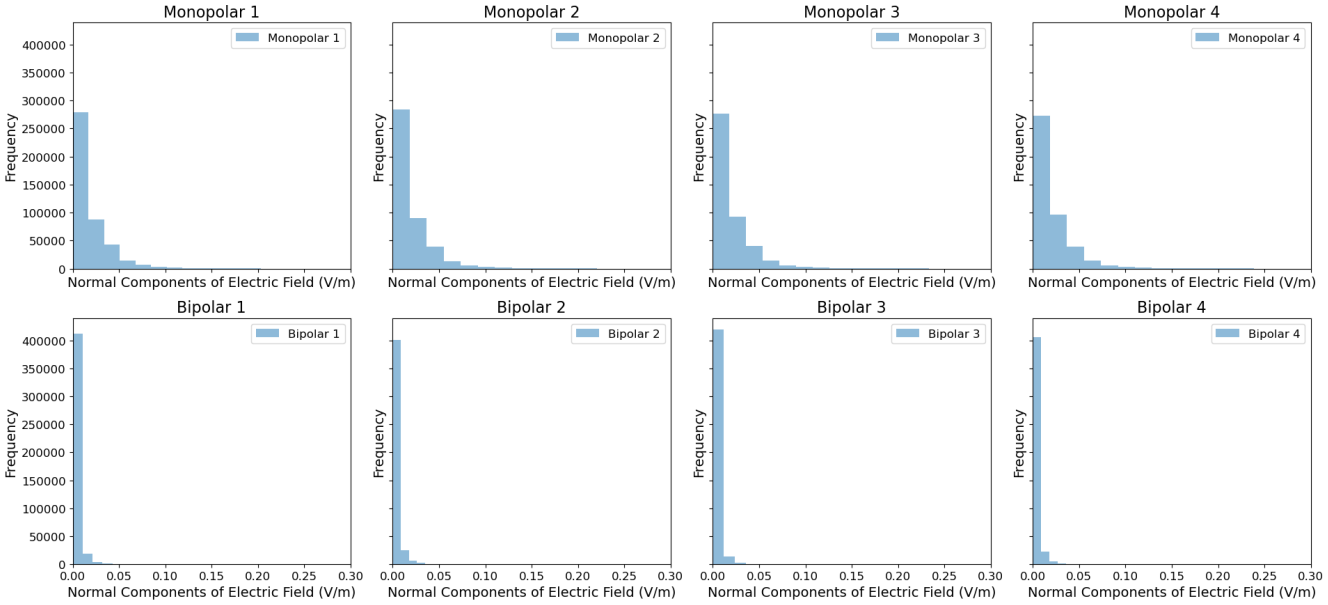

Figure 22: Histogram for the visualization of the distribution of the normal components of electric field for Premotor cortex for all simulations with the frequency of occurrence on the y-axis and the magnitude of electric field on the x-axis

The Precentral gyrus was chosen because of its proximity to the contacts, while the Premotor cortex, which is more distant from the contacts, plays an important role in the thalamocortical loop. Figure 18 shows the comparison between the Precentral gyrus and the Premotor cortex. The mean magnitude of the normal components of the electric field for Monopolar 4 is considerably higher in both regions. To visualize the distribution of the electric field in these regions,

histograms were plotted for the two regions as shown in figures 19, 20,21 and 22. Figures 19 and 20 show the magnitude of the electric field. Figures 21 and 22 show the distribution of the normal component of the electric field. The histograms show a uniform distribution for both regions. The histogram in Figures 19 and 21 shows the distribution of the magnitude of the electric field and the normal components of the electric field, respectively, for the Precentral gyrus for all simulations. Figures 20 and 22 show the distribution of the magnitude of the electric field and normal components of the electric field respectively for the Premotor cortex for all simulations.

8 Discussion

This study presents a novel approach to simulate Deep Brain Stimulation (DBS) by utilizing STL files of head segments and lead contacts. This model allows for better and more precise modeling of the electric field and current density distribution in cortical regions during DBS. In this study, the electric field generated in the cortical regions during DBS was simulated using FEMfuns. The model incorporated the contacts of the Medtronic 3389 lead model. The leads were positioned in the STN, a common target of a PD patient. The study was carried out by applying an input current of 1 mA per hemisphere (2 mA in total) for monopolar and bipolar stimulations. An increase in current intensity would proportionally increase the mean magnitude of the electric field and its normal components, leading to a corresponding increase in the electric field strength across the stimulated regions and vice versa [44]. After running the simulations for monopolar and bipolar simulations, the electric field data obtained for the entire head model was used to extract the electric field for the cortical regions. The results of this study provide an analysis of the electric field distributions in different brain regions for different monopolar and bipolar configurations.

Magnitude of Electric Field

The mean value of the magnitude of the electric field from monopolar configurations shows that it increases progressively from monopolar simulation 1 to monopolar simulation 4 in most regions, indicating increasing effects across different configurations. From Figure 10, it is visible that monopolar simulation 4 consistently shows the highest mean electric field values, suggesting that it might be the most effective monopolar configuration for stimulation within the simulations. Specifically, in the Precentral gyrus, the increase in the mean magnitude of electric field values from monopolar simulation 1 to monopolar simulation 4 is strong, highlighting the strong effect of monopolar 4 in this motor control region. Similarly, the Caudal and Inferior parietal cortex exhibit a progressive increase. Conversely, regions such as the Insula show less pronounced differences, indicating that monopolar simulation 1 or 2 might be sufficient for effective stimulation of the regions involved in the thalamocortical loop. The review of clinical studies on DBS by Rajamannar et al.[43] showed that the monopolar configuration has higher tissue activation, which aligns with the monopolar configuration that has a higher electric field for more regions compared to the bipolar configuration.

In bipolar configurations, the differences in the mean magnitude of the electric field between Bipolar simulations 1, 2, 3, and 4 are relatively small, indicating a more uniform effect across these configurations. Despite having a lower magnitude of electric field than monopolar configurations, the Precentral gyrus shows slight variations, with Bipolar simulations 2 and 4 having marginally higher values. The Inferior parietal cortex and the caudal regions also show a slight increase in the magnitude of electric field values within different bipolar configurations suggesting a modest but consistent effect of different bipolar settings.

Figure 18 shows the comparison between the Precentral gyrus and the Premotor Cortex, illustrating that the mean magnitude of the normal components of the electric field for monopolar simulation 4 is considerably higher in both regions. Specifically, the change in the magnitude of scalar products from bipolar simulation 4 to monopolar simulation 4 in the Premotor cortex is an increase of approximately 0.02 V/m, while the change in the Precentral gyrus is an increase of approximately 0.08 V/m. This indicates a stronger electric field effect for monopolar simulation 4 in both regions, with a more pronounced effect in the Precentral gyrus due to its proximity to the contact.

Distribution of Electric Fields

The distribution of the electric field for the Precentral gyrus and the Premotor cortex are shown in figures 19,20,21, and 22. From the histograms for the magnitude of the electric field for the Precentral gyrus and Premotor cortex 19,20, it can be seen that both monopolar and bipolar configurations have a uniform distribution of the electric field. Monopolar simulations have a wider distribution with a higher frequency of larger magnitudes of the electric field ranging from 0 V/m to 0.6 V/m for the Precentral gyrus and 0 V/m to 0.15 V/m for the Premotor cortex. The wider distribution for monopolar configuration suggests that it can influence more regions. The histograms for bipolar simulation show a narrower distribution with most of the electric field values centered at lower magnitudes. For the Precentral gyrus, the values range from 0 V/m to 0.4 V/m and from 0 V/m to 0.1 V/m for the Premotor cortex which can be seen in figures 19 and 20. Similar trends are observed for the normal components of the electric field.

So, bipolar simulations exhibit lower magnitudes of electric field and have a more localized simulation, which might be better suited for targeted stimulation, and monopolar configurations are more effective in inducing stronger electric fields within these motor-related regions and exhibit a broader range of high values, potentially leading to more extensive stimulation. This aligns with the studies from Rajamannar et al.[43], K A Sathi et al. [2] and, L Liu et al. [44]. The study of modeling and simulation of deep brain stimulation electrodes with various active contacts by K A Sathi discusses the differences in electric field distributions. It notes that monopolar configurations result in wider spreads of electric fields, while bipolar settings are more focused around the electrodes. L Liu in a pilot study investigating the impacts of stimulus parameters and configurations on motor cortex direct electrical stimulation, also found that bipolar stimulation generally produced more localized responses than monopolar stimulation.

The observations for monopolar and bipolar simulation from sections magnitude of electric field and distribution of electric field align with the hypothesis of monopolar simulations having higher magnitude of electric field for more regions compared to bipolar simulation. The monopolar simulation having a widespread and more extensive distribution compared to the bipolar simulation also aligns with the initial hypothesis. From the results of monopolar simulations, it can be seen that monopolar simulation 4 has a higher magnitude of electric field for most of the regions compared to other monopolar simulations making it a good choice for simulation for this study which aligns with the hypothesis.

From figure 15 showing the mean magnitude of the electric field to visualize a weak electric field, it can be seen that most of the regions selected away from the simulation site have a higher mean magnitude of the electric field for monopolar simulation compared to bipolar simulations. The mean magnitude of the electric field for monopolar configurations lies in a range of 0.1 V/m to 0.16 V/m. For bipolar configurations, the range is between 0.03 V/m to 0.06 V/m. Bipolar simulations 2 and 4 are found to have a higher magnitude of electric field in most of the regions. Within monopolar simulations, monopolar simulation 4 has the maximum mean magnitude of the electric field in most of the selected regions with a mean magnitude of the electric field above 0.12 V/m. Some regions like the Caudate, Insula, and Lingual cortex exhibit a higher magnitude for other monopolar simulations than for monopolar simulation 4. This is due to the positioning (proximity) of these regions to the lead and simulation site. So, monopolar simulation 4 has a higher magnitude of weak electric field which also aligns with the initial hypothesis.

Comparative Analysis of Monopolar and Bipolar Electric Field Simulations

From Table 3 and Figure 10 showing the mean magnitude of the electric field for selected cortical

regions, the variation in the monopolar configuration is between 0.0154 V/m and 0.2556 V/m with monopolar simulation 4 starting from 0.0174 V/m. The maximum value of the electric field for monopolar simulations varies between 0.2080 V/m and 3.13 V/m. For the maximum value of the electric field, most of the regions have a maximum value above 1 V/m. Some regions have a maximum value above 2 V/m as seen in table 5. For monopolar configurations 3 and 4 the number of regions with a maximum electric field above 2 V/m has also increased. The mean magnitude of the electric field for bipolar configuration is between 0.001 V/m and 0.12 V/m. The maximum value of the electric field ranges between 0.0182 V/m to 1.9373 V/m which can be seen in table 5. The maximum values for the simulations remain consistent across the bipolar simulations.

Experimental studies have placed the threshold for neuronal interaction with electric fields between 1 and 5 mV/mm [46]. The maximum value of each region shows that there is at least one or a few cells that can have the maximum values given in table 5. Most of the regions receive at least one cell with a maximum electric field of above 1 V/m for both monopolar and bipolar simulations. Monopolar simulations have regions with values above 2 V/m for some regions. Monopolar simulations 3 and 4 have more number of regions having a maximum electric field of more than 2 V/m. These values for maximum electric field indicate that there is at least a cell within these regions which has the possibility of causing neural modulation. From the value of maximum electric field, it is evident that monopolar simulations have higher values for most of the regions compared to bipolar simulations, making it more efficient to trigger neural responses.

Comparison of Simulation Result to tCS

Noninvasive brain stimulation such as tDCS / tACS is also used to study brain function, treat neurological and psychiatric disorders, and improve cognitive performance. For noninvasive brain stimulation, an input current of 1 to 2 mA is used as input current for clinical settings [30, 28, 31, 47]. Previous studies have shown that a current of 1 mA generates a maximum electric field ranging from 0.2 to 0.5 V/m within cortical regions, with most studies reporting maximum field strengths between 0.15 and 0.22 V/m [47, 48, 49]. This finding has been validated by a review study on electric field recordings conducted during in vivo tACS sessions [48]. In a randomized crossover trial, F. H. Kasten et al. [31] demonstrated the effectiveness of personalized transcranial alternating current stimulation (tACS) combined with physical therapy in improving motor and cognitive symptoms in patients with Parkinson's disease. Simulations conducted for each patient in this study revealed an average of the maximum electric field values of 0.13 ± 0.05 V/m within cortical regions, with maximum electric field strengths ranging to a maximum of 0.36 V/m. A previous study by U Pancholi et al. [50] analyzed the strengths and focality of the electric fields in subjects with healthy and neurologically impaired subjects under various tDCS protocols. It demonstrated that applying a 4mA current produced a maximum electric field strength between 0.425 and 0.766 V/m, with a mean magnitude ranging from 0.108 V/m to 0.217 V/m. This indicates that the mean magnitude of the electric field for 1 mA would range between 0.0270 V/m and 0.05425 V/m.

In the case of DBS, for the clinical treatment of Parkinson's disease, a current source of 1 mA to 4 mA per lead (per hemisphere) is applied to target the subthalamic nucleus and the Globus pallidus internus [5, 16]. This results in a total current of 2 to 8 mA across the entire brain. Simulations of this clinical setting can be performed by adjusting the input parameters in FEMfuns to match the desired current levels. For a 4 mA input current, the bipolar configuration produces a mean electric field magnitude ranging from 0.002 V/m to 0.2400 V/m, with maximum values between 0 and 4 V/m. In contrast, the monopolar configuration generates a mean

electric field magnitude between 0.0308 V/m and 0.5112 V/m, with maximum values reaching up to 6 V/m. within the cortical regions

For 1 mA of input current in tCS, within the critical regions, it generates a maximum electric field of 0.13 V/m, ranging from 0.08 to 0.36 V/m, and a mean magnitude of the electric field between 0.0270 and 0.05425 V/m. In contrast, DBS with a 4 mA input in the bipolar configuration produces a maximum field of up to 4 V/m (1 V/m per mA) and a mean magnitude of 0.002 to 0.2400 V/m (0.0005 to 0.06 V/m per mA). The monopolar DBS setup, with the same current, generates a higher maximum field of up to 6 V/m (1.5 V/m per mA) and a mean magnitude of 0.0308 to 0.5112 V/m (0.0077 to 0.128 V/m per mA). When considering the maximum values, DBS in both configurations produces maximum electric fields that are approximately 1 to slightly over 1 order of magnitude higher than those generated by tCS, indicating that DBS achieves significantly stronger maximum electric fields per unit of current within the cortical regions.

To compare the order of magnitude for the mean magnitudes of the electric field, average values of the range were taken. The average mean magnitude of the electric field in tCS is 0.040625 V/m. In comparison, DBS in the bipolar configuration produces an average mean magnitude of 0.03025 V/m per mA, which is slightly lower than that of tCS. However, in the monopolar configuration, DBS generates an average mean magnitude of 0.06775 V/m per mA, which is higher than that of tCS. When considering the per-unit current values, all three configurations fall within the same order of magnitude in terms of electric field strength per unit of current within the cortical regions. An order of magnitude comparison is made to evaluate whether DBS, despite being invasive, generates electric fields that are comparable to tCS, which has shown therapeutic potential in low-magnitude fields. This helps determine if DBS could similarly modulate neural activity and contribute to symptom reduction. The comparison is particularly crucial in the DECODE project, which explores the impact of weak cortical fields during DBS. By demonstrating that DBS can generate maximum electric fields slightly over one order of magnitude higher and mean magnitudes within the same order as those produced by tCS, the comparison supports the idea that even these weaker fields in DBS might subtly influence neural activity.

Limitations and Future Directions

This study focuses on a single lead placed in a specific location targeting the STN. Therefore, the results are not generalizable to other DBS simulations targeting different subcortical regions. So, a future direction would be to perform simulations using different leads, targets, and orientations. This helps us to understand the magnitude and distribution of electric fields for different settings.

Another limitation of the study is the incorporation of just the contacts for simulations. Instead of simulating DBS just with the contacts, including the insulator would give more precise electric field data. Incorporation of the lead can slightly influence the electric field values and can also influence the distribution of the electric field. This can be done as a continuation of this work in the future.

This study focused on developing a general head model. Only monopolar and bipolar simulations were carried out with anode and cathode assigned such that the currents are distributed uniformly and does not explore tripolar or quadripolar simulations, where three and four contacts are used, respectively. Additionally, it does not cover alternative monopolar simulations, where anodes can be assigned differently than those listed in Table 1, including wider monopolar configurations. Similarly, bipolar simulations could have anode-cathode assignments different

from those presented in Table 2. This can also be a future study. Future research could investigate these aspects as studied by K A Sathi et al. [2]. This study analyzes the electric field distribution for for leads with different combinations of active contacts to get optimum lead for greater therapeutic efficacy of the neurological patients.

Another limitation of the study is the time taken to calculate the normal components of the electric fields. Due to the complexity of the mesh, the calculation of normal components of the electric field takes approximately 33 to 40 hours which is not the ideal option. This calculation takes most of the time for all the simulations. In order to minimize the time consumption, the closest facet normals of the cells in the head mesh were calculated once and the data was saved which was used for other simulations. Since the same head model is used for all the simulations, the closest facet for each will remain the same. This was verified by calculating the normals for three simulations, followed by checking the normals for each facet cell by cell. This confirmed that the closest facet of each cell in the head model had the same values for all simulations. The initial try to calculate the normal components was carried out using Python broadcasting. It allows you to perform operations on arrays of different shapes in a memory-efficient way, without the need for explicit loops and speed up calculations. However, the head model used in the study, being very complex, was not able to calculate the normal components due to the requirement of every high internal memory. A different approach for calculating the normal components of the electric field was tried by using the k-dimensional tree (KD-tree). It is a data structure that is particularly well suited for organizing points in k-dimensional space, making it an efficient option for nearest-neighbor searches. This is an option to find the closest boundary facet for a given cell. This organizes the boundary midpoints into a tree structure, enabling efficient nearest-neighbor searches. It could calculate the normal components of the electric field in a very short time (15-20 minutes), but the visualization of the same showed some points that were not the normal components of the electric field. Using KD-tree would give normal components in a short time but it compromises the accuracy of the normal components being calculated. The initial method to calculate the normal components of the electric field was used for this study, as it gave accurate results and did not compromise on accuracy.

Another limitation of the study is the variability in the size of the mesh elements. The volumetric mesh was generated using Iso2Mesh, where only the maximum element volume could be specified during the mesh generation process. This function did not allow for uniform control over the element size throughout the mesh. As a result, the element size is not consistent across the entire mesh. Specifically, in regions near the contacts and boundaries, smaller elements may be necessary to accurately mesh these areas. This variability in element size should be taken into account when interpreting the results.

Another interesting direction would be to create a head model with the cortical parcellations from the MR data as the input. This can be achieved by using the STL files of the parcellated data as input for mesh generation. The different parcellated regions can be used by assigning different labels for each region. This can help to reduce the time for post-processing the data. This study focused on obtaining the electric field values for all of the cortical regions during DBS, which is computationally expensive. Making a head model with the STL files from cortical parcellation would help to obtain the electric field data for the specific regions directly using volume markers. It should be noted that it cannot provide GM as a whole as GM is divided into cortical regions. In order to get the data from gray matter the subcortical regions have to be merged, which can be done by creating a function for the same. A mesh with separate cortical regions along with a function to merge the STL files of the parcellation in FEMfuns makes the simulations less computationally expensive. Also, it can be used to for personalized

treatments as it can be used to get the electric field data for the specified regions which can help to tailor the stimulation settings.

9 Conclusion

This study provides a detailed analysis of electric field distributions across different brain regions under monopolar and bipolar Deep Brain Stimulation configurations. The analysis is based on a dataset from a Parkinson's Disease patient with DBS targeting the Subthalamic Nucleus using a Medtronic 3389 lead. The simulations were performed for a specific head model, focusing on particular stimulation settings as discussed in section 6.3. It is important to note that not all possible stimulation settings were tested in this study. The findings confirm that monopolar configurations generally produce stronger and more widespread electric fields compared to bipolar configurations, which exhibit a more localized and focused effect. Specifically within the cortical regions, monopolar DBS simulations generate mean electric fields that are comparable to, and in some cases exceed, those values typically observed in tCS. In contrast, bipolar DBS generally produces lower fields, but its maximum values can slightly exceed those seen in tCS. Despite these differences, both DBS configurations produce mean fields within the same order of magnitude as tCS within the cortical regions. However, within the cortical regions, the maximum fields in DBS, especially in monopolar configurations, are significantly higher, often by one or slightly more orders of magnitude. This suggests that DBS might also have the capability to subtly influence neural activity through its weaker fields similar to tCS. The results also demonstrate that varying the contact positions within the DBS lead significantly influences the magnitude and distribution of the electric fields within the cortical regions with certain contacts that potentially offer more optimal stimulation conditions. In monopolar simulation 4, using lead contact 3 results in a greater electric field magnitude compared to other monopolar and bipolar configurations. Moreover, progressively activating contacts from 0 to 3 leads to a consistent increase in the magnitude of the electric field. For bipolar configurations, a significant electric field magnitude is achieved when the cathode is placed at contact 3 and the anode at contact 1, or vice versa which are simulations 2 and 4 in this study.

Appendices

A Mesh Generation

Figure 23 shows the positioning of contacts in space. The visualization of contacts within the mesh is hard as they can be visualized with different cross sections of the mesh.

Figure 23: Visualization of contacts in space from the generated mesh visualized using gmsh

B Cortical parcellations

The output from the recon-all command shows the different parcellated regions with color coding as shown in Figure .

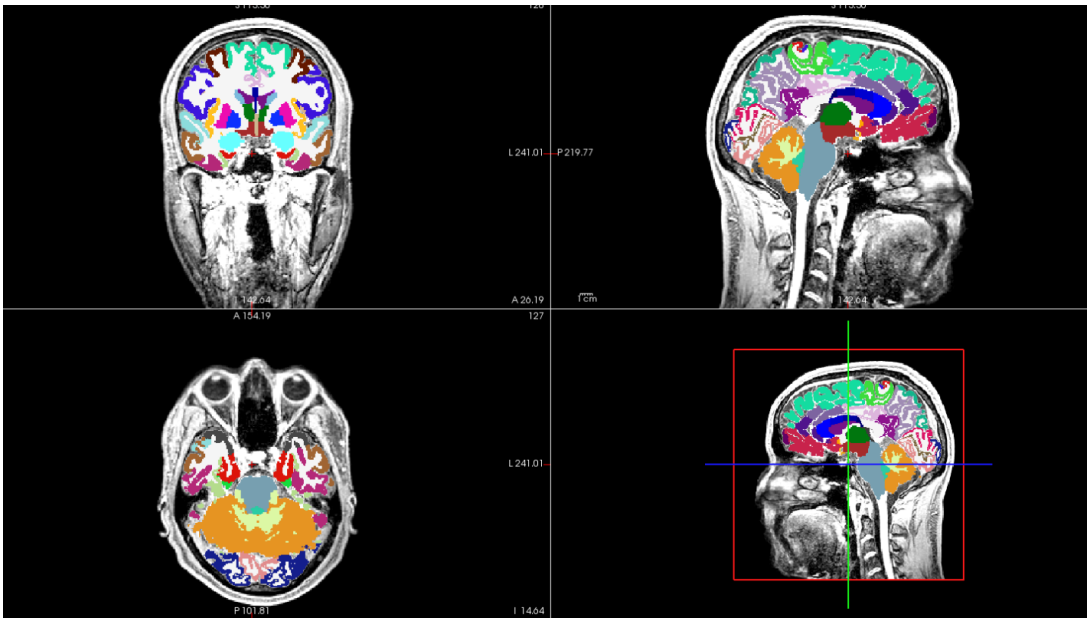

Figure 24: Output from recon-all command in FreeSurfer

The regions of the brain are color-coded and they can be seen in FreeSurfer to identify the regions corresponding to each region.

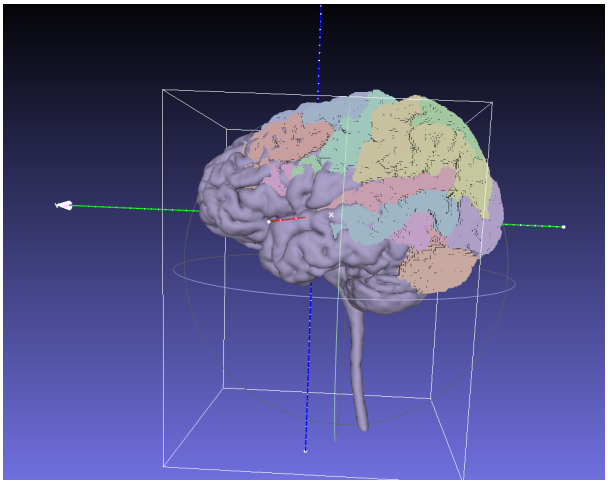

Figure 25: Parcellated data after registering with orig.mgz

In Figure 25, the gray matter is the gray matter from the head mesh, and different colored regions are the output from cortical parcellations. It can be seen that they are not aligned.

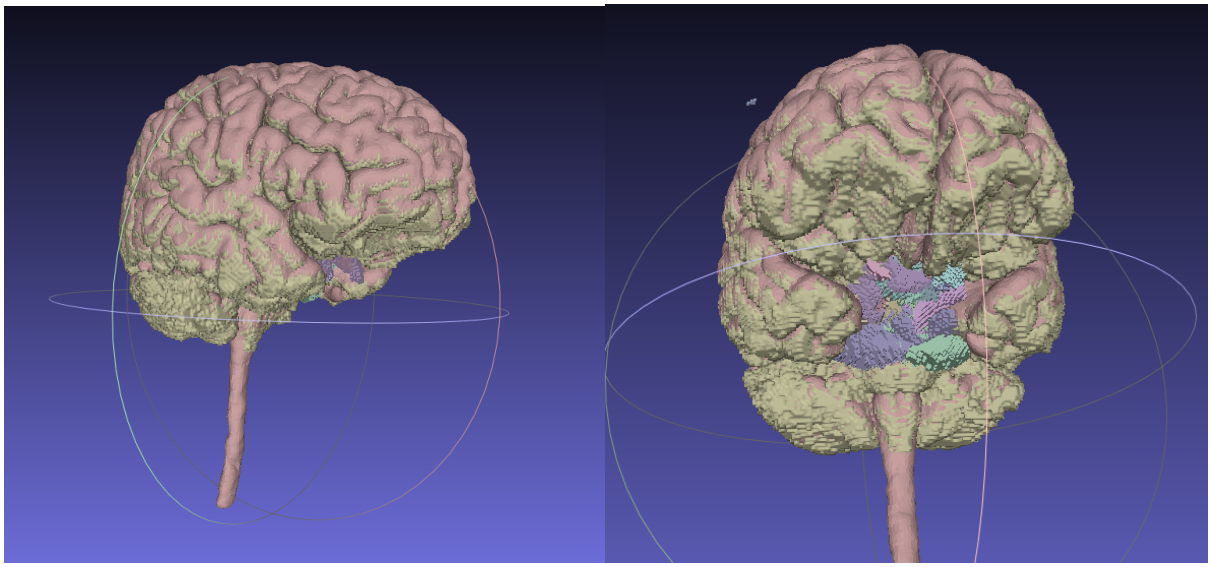

(a) (b)

Figure 26: Parcellated data after alignment using iterative closest point

C Simulations in FEMfuns

The conductivities and volume marker labels for regions used for simulations are given in table 9.

Contacts used in the simulations are numbered from 16 to 23. The numbering was initialized within Iso2mesh. Contacts 16 to 19 are from electrode one in the right hemisphere of the brain, and contacts 20 to 23 are contacts in the left hemisphere of the brain.

Table 9: Regions, Volume Markers and Conductivities (S/m) assigned for regions for for the study [3][4]

Regions	**Volume Marker**	**Conductivity (S/m)**
Skin	1	0.465
Skull	2	0.01
Cavity1	3	0.002
Cavity2	4	0.002
Cavity3	5	0.002
Cavity4	6	0.002
Cavity5	7	0.002
Cavity6	8	0.002
Cavity7	9	0.002
Cyeball1	10	0.5
Cyeball2	11	0.5
Ventricles	12	1.654
Cerebrospinal Fluid	13	1.654
Gray Matter	14	0.276
White Matter	15	0.126
Contact1	16	8.9e6
Contact2	17	8.9e6
Contact3	18	8.9e6
Contact4	19	8.9e6
Contact5	20	8.9e6
Contact6	21	8.9e6
Contact7	22	8.9e6
Contact8	23	8.9e6

Table 10: Table of Contacts Coordinates

Contacts	X (mm)	Y (mm)	Z (mm)
Contact 16	10.652	-13.418	-10.715
Contact 17	11.355	-12.843	-8.800
Contact 18	12.058	-12.266	-6.869
Contact 19	12.753	-11.692	-4.955
Contact 20	-11.079	-14.253	-10.817
Contact 21	-11.856	-13.563	-9.008
Contact 22	-12.630	-12.875	-7.202
Contact 23	-13.406	-12.184	-5.393

D Visualization of electric field

The visualization of the electric field for monopolar and bipolar simulation in coronal view is given in this section. Figure 27a shows the distribution of electric field for monopolar configuration in coronal view.

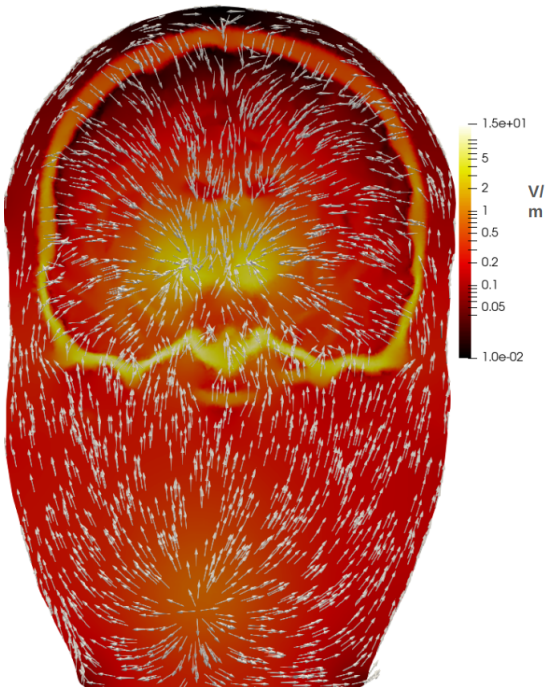

(a) The visualization of electric field for monopolar configuration in coronal view. The arrows represent the flow of the electric field.

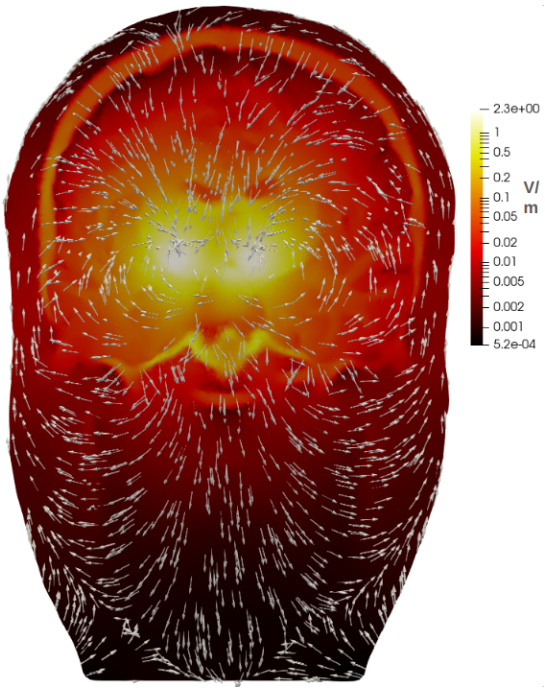

(b) The visualization of electric field for bipolar configuration in coronal view. The arrows represent the flow of the electric field.

Figure 27: Electric field visualization in coronal view for monopolar (left) and bipolar (right) configurations.

E Electric field data from cortical parcellation

The electric field data for regions from cortical parcellation are given in this section. Names of the region in the figures shown are according to the names obtained from cortical parcellation. Table 11 shows the mapping of the cortical parcellation names to the anatomical names of the region.

Region Name From FreeSurfer	Mapped Anatomical Region Name
CC_Anterior_surface	Corpus Callosum Anterior
CC_Central_surface	Corpus Callosum Central
CC_Mid_Anterior_surface	Corpus Callosum Mid Anterior
CC_Mid_Posterior_surface	Corpus Callosum Mid Posterior
CC_posterior_surface	Corpus Callosum Posterior
accumbensarea	Accumbens Area
amygdala	Amygdala
auditorycortex	Auditory Cortex
bankssts	Banks of the Superior Temporal Sulcus
caudalanteriorcingulate	Caudal Anterior Cingulate
caudalmiddlefrontal	Caudal Middle Frontal Cortex
caudate	Caudate
cerebellumcortex	Cerebellar Cortex
choroidplexus	Choroid Plexus
cuneus	Cuneus
entorhinal	Entorhinal Cortex
frontalpole	Frontal Pole
fusiform	Fusiform Cortex
hippocampus	Hippocampus
inferiortemporal	Inferior Temporal Cortex
inferiorparietal	Inferior Parietal Cortex
insula	Insula
isthmuscingulate	Isthmus of the Cingulate Cortex
lateraloccipital	Lateral Occipital Cortex
lateralorbitofrontal	Lateral Orbitofrontal Cortex
lingual	Lingual Cortex
mediotemporal	Medial Orbitofrontal Cortex
middletemporal	Middle Temporal Cortex
pallidum	Pallidum
paracentral	Paracentral Lobule
parahippocampal	Parahippocampal Cortex
parsopercularis	Pars Opercularis
parsorbitalis	Pars Orbitalis
parstriangularis	Pars Triangularis
pericalcarine	Pericalcarine Cortex
postcentral	Postcentral Gyrus
posteriorcingulate	Posterior Cingulate Cortex
precentral	Precentral Gyrus
precuneus	Precuneus
rostralanteriorcingulate	Rostral Anterior Cingulate Cortex
rostralmiddlefrontal	Rostral Middle Frontal Cortex
superiorfrontal	Superior Frontal Cortex
superiorparietal	Superior Parietal Cortex
superiortemporal	Superior Temporal Cortex
supramarginal	Supramarginal Gyrus
thalamus	Thalamus
ventraldc	Ventral Diencephalon

Table 11: Region Names Mapping

E.1 Mean magnitude of electric field for regions from cortical parcellations

Table 12: Mean magnitude of the electric field by Region and Simulation. 'Bi' denotes bipolar simulations, and 'Mono' denotes monopolar simulations. The simulation numbers correspond to those detailed in Tables 1 and 2

Region	**Bi 1**	**Bi 2**	**Bi 3**	**Bi 4**	**Mono 1**	**Mono 2**	**Mono 3**	**Mono 4**
					V/m			
Corpus Callosum Anterior	0.1011	0.1128	0.1011	0.1128	0.1932	0.2219	0.2448	0.2564
Corpus Callosum Central	0.0818	0.0959	0.0818	0.0959	0.1488	0.1764	0.2074	0.2358
Corpus Callosum Mid Anterior	0.0328	0.0378	0.0328	0.0378	0.0942	0.1052	0.1172	0.1294
Corpus Callosum Mid Posterior	0.0652	0.0714	0.0652	0.0714	0.1565	0.1788	0.1988	0.2125
Corpus Callosum Posterior	0.0350	0.0350	0.0350	0.0350	0.1305	0.1361	0.1394	0.1406
Accumbens Area	0.0892	0.0990	0.0892	0.0990	0.1784	0.1999	0.2152	0.2209
Amygdala	0.1144	0.1343	0.1144	0.1343	0.2082	0.2408	0.2725	0.2981
Auditory Cortex	0.0022	0.0024	0.0022	0.0024	0.0154	0.0160	0.0166	0.0173
Banks of the Superior Temporal Sulcus	0.0800	0.0840	0.0800	0.0840	0.1739	0.1821	0.1889	0.1929
Caudal Anterior Cingulate	0.0596	0.0696	0.0596	0.0696	0.1353	0.1517	0.1698	0.1876
Caudal Middle Frontal Cortex	0.0476	0.0516	0.0476	0.0516	0.1184	0.1312	0.1443	0.1565
Caudate	0.0387	0.0353	0.0387	0.0353	0.1193	0.1137	0.1083	0.1036
Cerebellar Cortex	0.0765	0.0745	0.0765	0.0745	0.1807	0.1776	0.1747	0.1709
Choroid Plexus	0.0218	0.0247	0.0218	0.0247	0.0886	0.0954	0.1014	0.1058
Cuneus	0.0490	0.0518	0.0490	0.0518	0.1269	0.1393	0.1507	0.1596
Entorhinal Cortex	0.0659	0.0694	0.0659	0.0694	0.1501	0.1546	0.1584	0.1604
Frontal Pole	0.0548	0.0562	0.0548	0.0562	0.1413	0.1442	0.1463	0.1467
Fusiform Cortex	0.0552	0.0607	0.0552	0.0607	0.1314	0.1386	0.1449	0.1508
Hippocampus	0.1237	0.1400	0.1237	0.1400	0.2629	0.2911	0.2964	0.2815
Inferior Temporal Cortex	0.0851	0.0847	0.0851	0.0847	0.2101	0.2157	0.2142	0.2063
Inferior Parietal Cortex	0.0760	0.0784	0.0760	0.0784	0.1748	0.1804	0.1858	0.1896
Insula	0.0427	0.0416	0.0427	0.0416	0.1199	0.1194	0.1185	0.1165
Isthmus of the Cingulate Cortex	0.0651	0.0666	0.0651	0.0666	0.1532	0.1597	0.1653	0.1679
Lateral Occipital Cortex	0.0616	0.0659	0.0616	0.0659	0.1432	0.1521	0.1605	0.1663
Lateral Orbitofrontal Cortex	0.0590	0.0651	0.0590	0.0651	0.1313	0.1454	0.1572	0.1637
Lingual Cortex	0.0465	0.0466	0.0465	0.0466	0.1223	0.1270	0.1289	0.1268
Medial Orbitofrontal Cortex	0.0900	0.0948	0.0900	0.0948	0.1926	0.2025	0.2106	0.2150
Middle Temporal Cortex	0.1108	0.1186	0.1108	0.1186	0.2213	0.2542	0.2767	0.2814
Pallidum	0.0849	0.0976	0.0849	0.0976	0.1740	0.2001	0.2247	0.2429
Paracentral Lobule	0.0546	0.0562	0.0546	0.0562	0.1294	0.1396	0.1481	0.1526
Parahippocampal Cortex	0.0391	0.0410	0.0391	0.0410	0.1105	0.1204	0.1298	0.1374
Pars Opercularis	0.0835	0.0929	0.0835	0.0929	0.1664	0.1855	0.2034	0.2156
Pars Orbitalis	0.0574	0.0634	0.0574	0.0634	0.1328	0.1524	0.1724	0.1896
Pars Triangularis	0.0695	0.0682	0.0695	0.0682	0.1625	0.1570	0.1532	0.1501
Pericalcarine Cortex	0.0446	0.0485	0.0446	0.0485	0.1146	0.1256	0.1354	0.1425
Postcentral Gyrus	0.0455	0.0463	0.0455	0.0463	0.1149	0.1159	0.1169	0.1172
Posterior Cingulate Cortex	0.0759	0.0744	0.0759	0.0744	0.1803	0.1747	0.1705	0.1674
Precentral Gyrus	0.0969	0.1099	0.0969	0.1099	0.1786	0.2063	0.2350	0.2556
Precuneus	0.0478	0.0506	0.0478	0.0506	0.1240	0.1284	0.1324	0.1354
Premotor Cortex	0.0052	0.0055	0.0052	0.0055	0.0278	0.0284	0.0291	0.0297
Putamen	0.0786	0.0922	0.0786	0.0922	0.1545	0.1762	0.1979	0.2163
Rostral Middle Frontal Cortex	0.0462	0.0462	0.0462	0.0462	0.1269	0.1277	0.1288	0.1299
Rostral Anterior Cingulate Cortex	0.0321	0.0329	0.0321	0.0329	0.0951	0.0955	0.0963	0.0972
Superior Parietal Cortex	0.0800	0.0790	0.0800	0.0790	0.1813	0.1792	0.1779	0.1756
Superior Temporal Cortex	0.0576	0.0605	0.0576	0.0605	0.1328	0.1469	0.1606	0.1702
Superior Frontal Cortex	0.0452	0.0479	0.0452	0.0479	0.1148	0.1213	0.1274	0.1319
Supramarginal Gyrus	0.0526	0.0554	0.0526	0.0554	0.1281	0.1455	0.1611	0.1720
Thalamus	0.0499	0.0515	0.0499	0.0515	0.1299	0.1412	0.1497	0.1543
Ventral Diencephalon	0.0415	0.0394	0.0415	0.0394	0.0996	0.1029	0.1077	0.1130

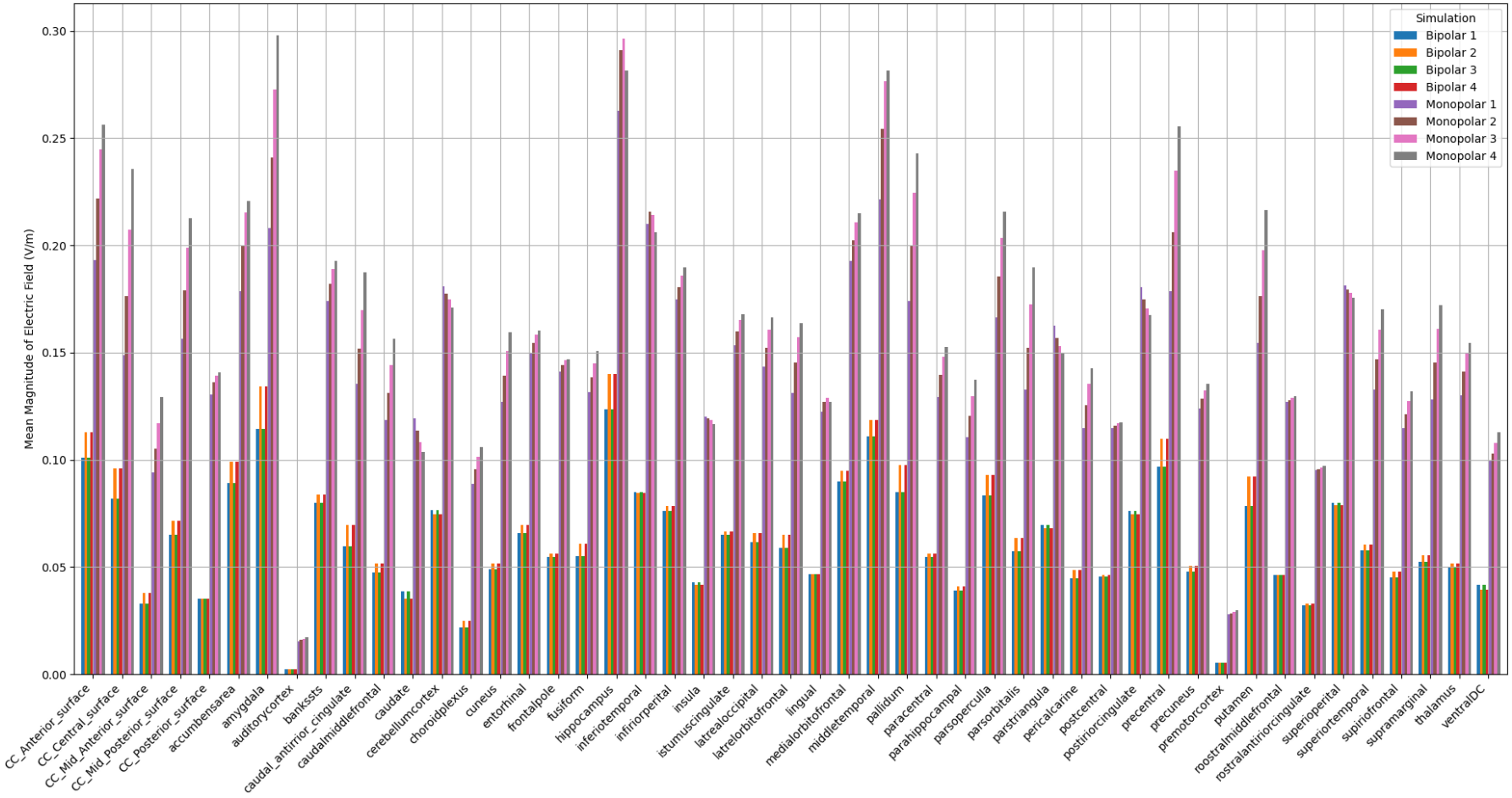

Figure 28: Mean magnitude of electric field Values by Brain Region and Simulation

E.2 Maximum values for electric field magnitude in regions from cortical parcellations

Table 13: Maximum value of electric field by Region and Simulation. 'Bi' denotes bipolar simulations, and 'Mono' denotes monopolar simulations. The simulation numbers correspond to those detailed in Tables 1 and 2

Region	Bi 1	Bi 2	Bi 3	Bi 4	Mono 1	Mono 2	Mono 3	Mono 4
					V/m			
Corpus Callosum Anterior	0.76216	0.91836	0.76215	0.91836	1.31410	1.36240	1.29330	1.17090
Corpus Callosum Central	0.71181	0.77666	0.71179	0.77666	0.66511	0.87615	1.18320	1.33690
Corpus Callosum Mid Anterior	0.14439	0.18366	0.14439	0.18366	0.19525	0.24224	0.30943	0.39317
Corpus Callosum Mid Posterior	0.59970	0.66826	0.59968	0.66826	0.90587	1.11890	1.16930	1.19350
Corpus Callosum Posterior	0.16208	0.18190	0.16208	0.18190	0.51992	0.55445	0.55203	0.50523
Accumbens Area	1.89700	2.54900	1.89700	2.54900	1.90850	2.71140	3.10650	3.50410
Amygdala	1.89700	2.54900	1.89700	2.54900	2.04460	2.71140	3.10650	3.51020
Auditory Cortex	0.03635	0.03808	0.03635	0.03808	0.22365	0.22262	0.22137	0.22006
Banks of the Superior Temporal Sulcus	2.57640	2.41300	2.57640	2.41300	3.91240	2.71140	2.94610	3.43980
Caudal Anterior Cingulate	1.71150	2.54900	1.71150	2.54900	0.89824	1.50260	2.54250	3.51020
Caudal Middle Frontal Cortex	0.23420	0.30620	0.23420	0.30620	0.52527	0.52710	0.55656	0.59707
Caudate	2.79440	2.26250	2.79440	2.26250	3.91080	2.97240	3.10650	3.34560
Cerebellar Cortex	2.79440	2.38350	2.79440	2.38350	3.91080	2.71140	3.10650	3.51020
Choroid Plexus	0.06419	0.08706	0.06419	0.08706	0.17247	0.18666	0.19923	0.21255
Cuneus	0.31226	0.32480	0.31226	0.32480	0.59804	0.63824	0.76736	0.81092
Entorhinal Cortex	1.89700	2.13940	1.89700	2.13940	2.04460	2.53750	3.10650	3.26020
Frontal Pole	1.89700	2.38870	1.89700	2.38870	2.04460	2.71140	3.10650	3.47290
Fusiform Cortex	1.62400	2.41230	1.62400	2.41230	2.04460	2.71140	2.78550	3.51020
Hippocampus	0.89379	1.26060	0.89380	1.26060	1.90820	2.00260	1.60410	1.39590
Inferior Temporal Cortex	1.40830	1.42180	1.40830	1.42180	2.04460	2.71140	2.68130	2.12230
Inferior Parietal Cortex	2.45430	2.54900	2.45430	2.54900	3.67330	2.71140	3.10650	3.51020
Insula	1.89700	2.38870	1.89700	2.38870	1.96000	2.43140	3.10650	3.51020
Isthmus of the Cingulate Cortex	1.82620	2.54900	1.82620	2.54900	2.04460	2.44070	2.94610	3.51020
Lateral Occipital Cortex	1.89700	2.38350	1.89700	2.38350	2.04090	2.71140	3.10650	3.51020
Lateral Orbitofrontal Cortex	1.89700	2.41300	1.89700	2.41300	2.04460	2.71140	3.10650	3.51020
Lingual Cortex	1.89700	2.13940	1.89700	2.13940	2.04460	2.71140	3.10650	3.17740
Medial Orbitofrontal Cortex	1.51560	2.38870	1.51560	2.38870	2.04090	2.24130	2.31360	3.39510
Middle Temporal Cortex	1.89700	2.13940	1.89700	2.13940	2.04090	2.71140	3.10650	3.26020
Pallidum	1.89700	2.38870	1.89700	2.38870	2.04460	2.71140	3.10650	3.51020
Paracentral Lobule	1.26050	1.22780	1.26050	1.22780	1.87440	2.53180	2.52610	2.00280
Parahippocampal Cortex	0.31915	0.39449	0.31915	0.39449	0.48711	0.54119	0.68987	0.78268
Pars Opercularis	1.89700	2.41300	1.89700	2.41300	2.04460	2.71140	3.10650	3.51020
Pars Orbitalis	0.75837	1.09280	0.75836	1.09280	0.78943	0.98378	1.28950	1.66940
Pars Triangularis	1.89700	2.38870	1.89700	2.38870	2.83960	2.53750	3.10650	3.51020
Pericalcarine Cortex	0.98553	1.02910	0.98552	1.02910	1.47970	1.56520	1.65690	1.91380
Postcentral Gyrus	2.31810	2.54900	2.31810	2.54900	3.33490	2.53750	2.88570	3.51020
Posterior Cingulate Cortex	1.89700	2.38350	1.89700	2.38350	2.70880	2.71140	3.10650	3.47290
Precentral Gyrus	1.89700	2.35980	1.89700	2.35980	1.65450	2.22280	3.10650	3.35230
Precuneus	1.79690	2.54900	1.79690	2.54900	2.04460	2.71140	2.83460	3.51020
Premotor Cortex	0.56385	0.43881	0.56385	0.43881	0.86688	0.96308	0.95533	0.83310
Putamen	1.89700	2.54900	1.89700	2.54900	2.04460	2.71140	3.10650	3.51020
Rostral Middle Frontal Cortex	1.79690	2.54900	1.79690	2.54900	2.04460	2.44070	2.83460	3.51020
Rostral Anterior Cingulate Cortex	1.89700	2.54900	1.89700	2.54900	2.62890	2.71140	3.10650	3.51020
Superior Parietal Cortex	1.89700	2.41230	1.89700	2.41230	2.49060	2.44070	3.10650	3.51020
Superior Temporal Cortex	1.40630	1.06960	1.40630	1.06960	1.35930	2.05650	2.54470	2.18110
Superior Frontal Cortex	1.70810	1.72930	1.70810	1.72930	1.91860	2.53750	2.69190	2.92220
Supramarginal Gyrus	0.53934	0.58050	0.53933	0.58050	0.74142	0.90281	1.03670	1.17960
Thalamus	0.84099	0.85152	0.84097	0.85152	1.39650	1.59640	1.64340	1.55190
Ventral Diencephalon	0.20277	0.15278	0.20277	0.15278	0.47761	0.36705	0.28212	0.33382

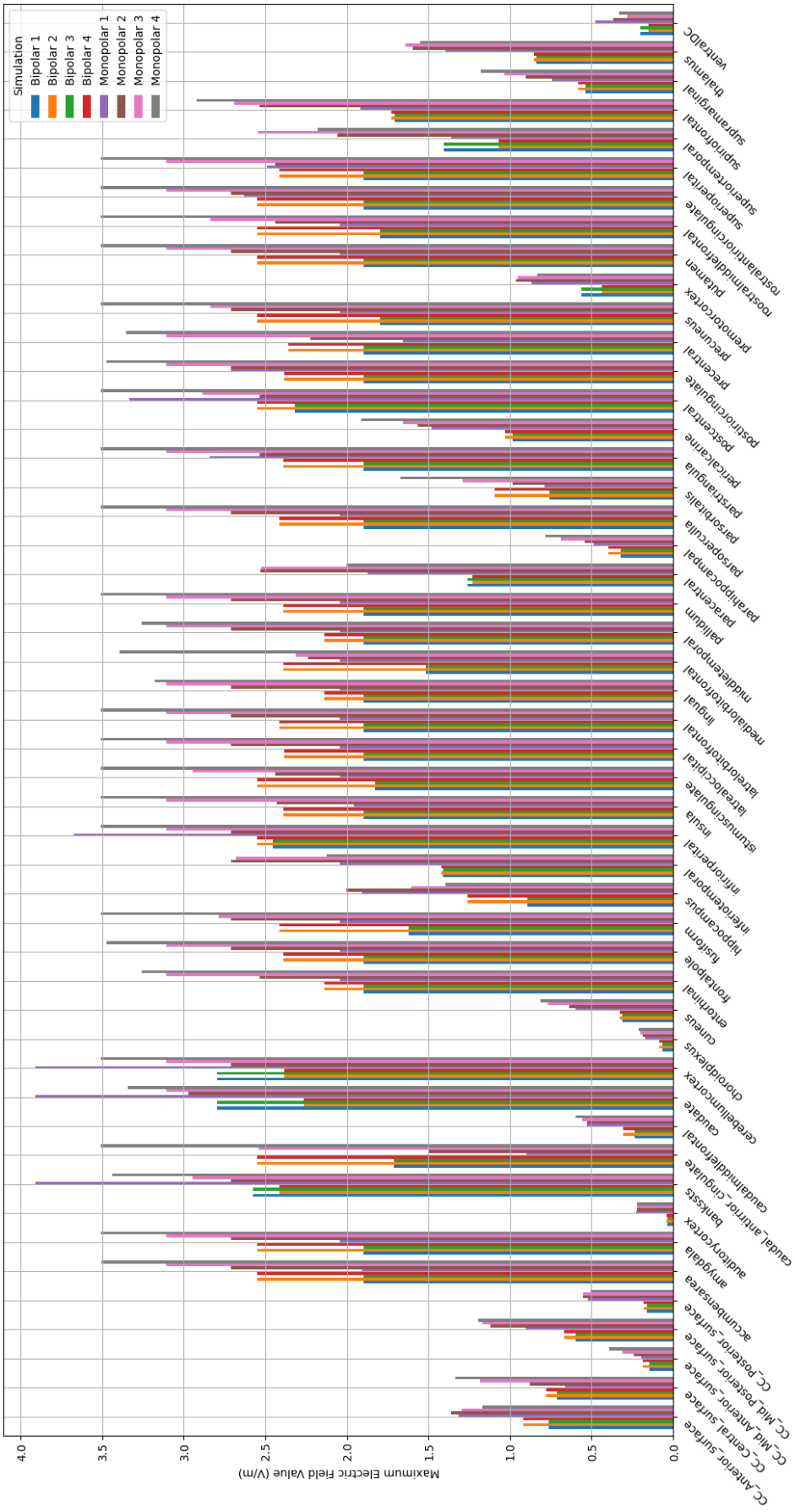

Figure 29: Maximim values of the magnitude of electric field by Brain Region and Simulation

E.3 Maximum values for electric field magnitude in regions from cortical parcellations after taking 99.9th percentile of the electric field

Table 14: Maximum values for electric field by Region and Simulation excluding 99.9th Percentile. 'Bi' denotes bipolar simulations, and 'Mono' denotes monopolar simulations. The simulation numbers correspond to those detailed in Tables 1 and 2

Region	Bi 1	Bi 2	Bi 3	Bi 4	Mono 1	Mono 2	Mono 3	Mono 4
					V/m			
Corpus Callosum Anterior	0.67417	0.77820	0.67418	0.77820	1.13490	1.27390	1.13870	1.13720
Corpus Callosum Central	0.66623	0.70691	0.66622	0.70691	0.58070	0.78996	1.09720	1.24400
Corpus Callosum Mid Anterior	0.12701	0.16293	0.12701	0.16293	0.18346	0.23437	0.29054	0.35837
Corpus Callosum Mid Posterior	0.52279	0.60386	0.52278	0.60386	0.74924	0.90477	0.99919	1.06550
Corpus Callosum Posterior	0.15360	0.16495	0.15360	0.16495	0.48711	0.48191	0.47081	0.42618
Accumbens Area	1.62400	1.86340	1.62400	1.86340	1.64810	2.14380	2.66940	3.08820
Amygdala	1.58760	2.09300	1.58760	2.09300	1.71720	2.10660	2.54250	3.13040
Auditory Cortex	0.02229	0.02445	0.02229	0.02445	0.10192	0.10308	0.10345	0.10424
Banks of the Superior Temporal Sulcus	1.56400	1.43440	1.56400	1.43440	2.37320	2.05770	2.30540	2.37810
Caudal Anterior Cingulate	1.24000	1.94070	1.24000	1.94070	0.70454	1.07650	1.87600	2.87410
Caudal Middle Frontal Cortex	0.21280	0.26101	0.21280	0.26101	0.47513	0.48071	0.46651	0.54863
Caudate	1.46330	1.12850	1.46330	1.12850	2.26950	1.78420	1.52200	1.27660
Cerebellar Cortex	1.61730	1.43490	1.61730	1.43490	2.21700	1.90970	2.20680	2.30400
Choroid Plexus	0.06356	0.08667	0.06356	0.08667	0.16250	0.17569	0.18710	0.20806
Cuneus	0.27774	0.28136	0.27773	0.28136	0.55355	0.61077	0.66358	0.71148
Entorhinal Cortex	1.29730	1.55590	1.29730	1.55590	1.55890	1.83230	2.16730	2.45870
Frontal Pole	1.17890	1.52780	1.17890	1.52780	1.48310	1.78210	2.03110	2.30800
Fusiform Cortex	1.08460	1.46120	1.08460	1.46120	1.53230	1.78210	1.87190	2.22120
Hippocampus	0.78814	1.11030	0.78813	1.11030	1.64810	1.79650	1.56570	1.31730
Inferior Temporal Cortex	1.11890	1.16970	1.11890	1.16970	1.72990	2.08470	2.14270	1.65350
Inferior Parietal Cortex	1.43270	1.77470	1.43270	1.77470	1.76070	1.98240	2.20600	2.69020
Insula	1.00830	1.09350	1.00830	1.09350	1.28650	1.39930	1.72530	1.78240
Isthmus of the Cingulate Cortex	1.31680	1.62020	1.31680	1.62020	1.38090	1.69010	2.13160	2.52640
Lateral Occipital Cortex	1.27030	1.58090	1.27030	1.58090	1.54740	1.88330	2.17490	2.45220
Lateral Orbitofrontal Cortex	1.47990	1.68270	1.47980	1.68270	1.65810	2.05770	2.46650	2.69020
Lingual Cortex	1.11890	1.17110	1.11890	1.17110	1.48310	1.79160	2.00390	1.78240
Medial Orbitofrontal Cortex	1.14140	1.52520	1.14140	1.52520	1.55390	1.59020	1.83390	2.37810
Middle Temporal Cortex	1.51960	1.59190	1.51960	1.59190	1.76940	2.21300	2.58730	2.62840
Pallidum	1.50610	1.87660	1.50610	1.87660	1.62210	2.08510	2.48760	2.92220
Paracentral Lobule	0.80825	0.92452	0.80825	0.92452	1.36070	1.53510	1.56570	1.42500
Parahippocampal Cortex	0.26593	0.30939	0.26593	0.30939	0.42740	0.49832	0.59144	0.68195
Pars Opercularis	1.46160	1.93730	1.46160	1.93730	1.67940	1.97610	2.34630	2.95760
Pars Orbitalis	0.58809	0.88915	0.58809	0.88915	0.57148	0.73997	1.00550	1.44210
Pars Triangularis	1.37730	1.56840	1.37730	1.56840	1.71720	1.84060	2.17350	2.45870
Pericalcarine Cortex	0.62982	0.75201	0.62982	0.75201	1.06070	1.18990	1.17020	1.27630
Postcentral Gyrus	1.18700	1.28460	1.18700	1.28460	1.52080	1.59900	1.87980	2.00280
Posterior Cingulate Cortex	1.22570	1.38450	1.22560	1.38450	1.76930	1.69260	1.94430	2.21420
Precentral Gyrus	1.56400	1.93730	1.56400	1.93730	1.33540	1.87660	2.51270	2.95760
Precuneus	1.11970	1.47410	1.11970	1.47410	1.43980	1.61430	1.92760	2.28150
Premotor Cortex	0.18418	0.18468	0.18417	0.18468	0.49200	0.46488	0.41707	0.36758
Putamen	1.43270	1.86450	1.43270	1.86450	1.60300	1.96290	2.34400	2.85540
Rostral Middle Frontal Cortex	1.07220	1.29530	1.07210	1.29530	1.41290	1.35060	1.63000	2.17680
Rostral Anterior Cingulate Cortex	1.06140	1.30830	1.06140	1.30830	1.30260	1.39370	1.77230	2.12850
Superior Parietal Cortex	1.34390	1.63950	1.34390	1.63950	1.54560	1.67950	2.15370	2.59830
Superior Temporal Cortex	0.63908	0.71703	0.63907	0.71703	0.70491	0.87398	1.09720	1.30460
Superior Frontal Cortex	0.92993	1.15700	0.92993	1.15700	1.26570	1.38200	1.57880	1.87000
Supramarginal Gyrus	0.44787	0.46306	0.44786	0.46306	0.64083	0.73519	0.87308	0.99531
Thalamus	0.51032	0.62724	0.51032	0.62724	1.11970	1.25770	1.16950	1.02190
Ventral Diencephalon	0.17326	0.13941	0.17326	0.13941	0.39874	0.31358	0.27192	0.29786

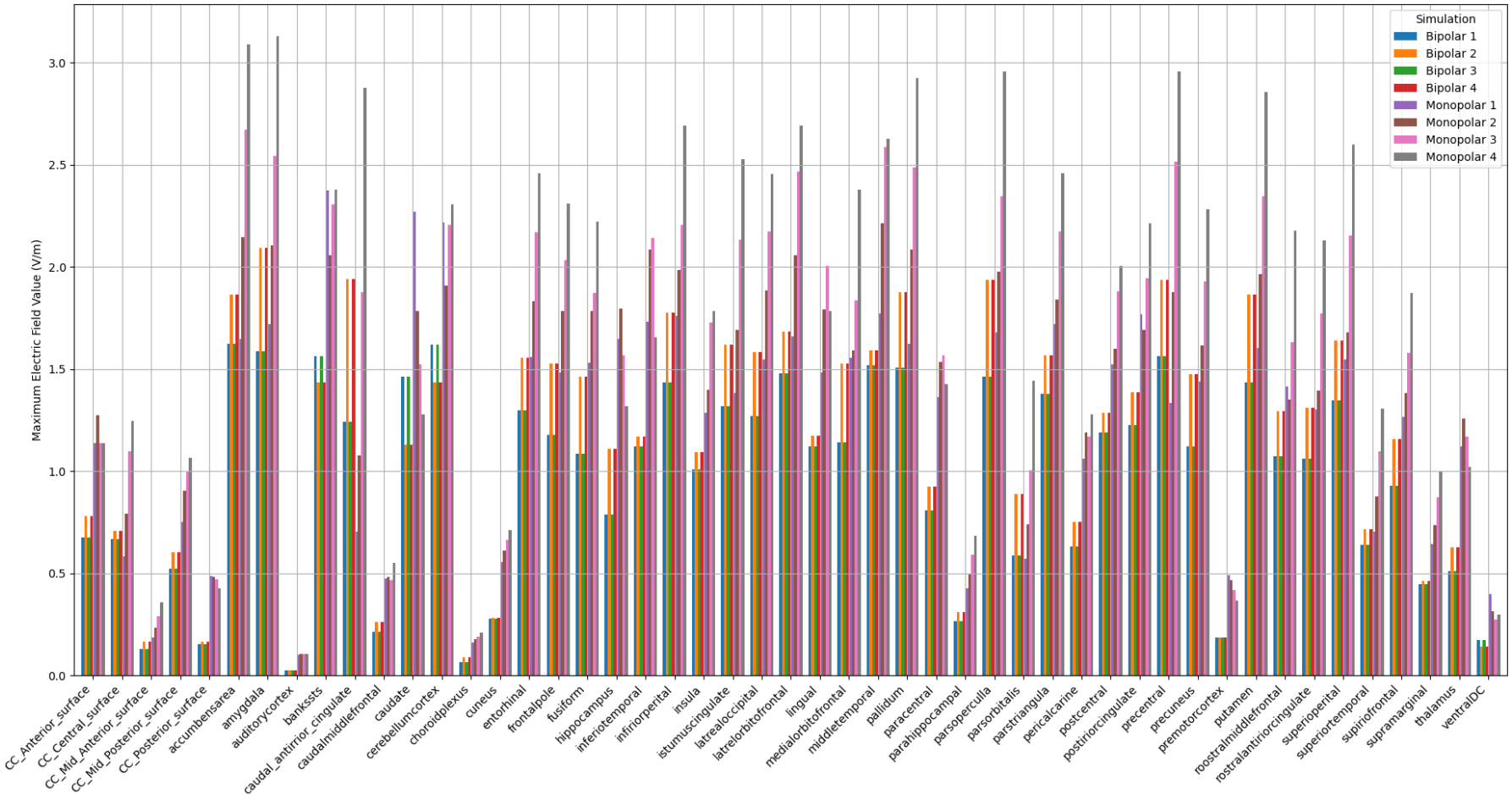

Figure 30: Maximim values of the magnitude of EF by Brain Region and Simulation after taking 99.9th percentile

E.4 Normal components of Electric field

Table 15: Mean magnitude of normal components of electric field by Region and Simulation. 'Bi' denotes bipolar simulations, and 'Mono' denotes monopolar simulations. The simulation numbers correspond to those detailed in Tables 1 and 2

Region	Bi 1	Bi 2	Bi 3	Bi 4	Mono 1	Mono 2	Mono 3	Mono 4
				V/m				
Corpus Callosum Anterior	0.053283	0.061191	0.052171	0.061288	0.134929	0.150074	0.157914	0.158572
Corpus Callosum Central	0.036866	0.044083	0.046484	0.052690	0.087429	0.099817	0.113392	0.125386
Corpus Callosum Mid Anterior	0.020017	0.021699	0.020247	0.025214	0.079835	0.086234	0.092143	0.096820
Corpus Callosum Mid Posterior	0.035056	0.037971	0.044395	0.045397	0.114455	0.126858	0.136928	0.142703
Corpus Callosum Posterior	0.021105	0.020936	0.033928	0.034675	0.124867	0.125593	0.123757	0.120568
Accumbens Area	0.040401	0.045590	0.054880	0.059451	0.117549	0.125440	0.127410	0.125422
Amygdala	0.053356	0.059218	0.061066	0.066792	0.123749	0.138854	0.149243	0.154559
Auditory Cortex	0.001476	0.001574	0.001434	0.001522	0.009619	0.009975	0.010395	0.010835
Banks of the Superior Temporal Sulcus	0.041699	0.043491	0.050694	0.051821	0.121366	0.123025	0.122242	0.120260
Caudal Anterior Cingulate	0.027588	0.031701	0.036166	0.038220	0.084596	0.091217	0.097491	0.103394
Caudal Middle Frontal Cortex	0.025733	0.027262	0.035349	0.037892	0.090088	0.095413	0.099996	0.103739
Caudate	0.023330	0.020546	0.024848	0.022596	0.080467	0.076347	0.071770	0.067609
Cerebellar Cortex	0.041690	0.039806	0.046536	0.043165	0.120361	0.115564	0.110093	0.104752
Choroid Plexus	0.014159	0.015357	0.014176	0.017466	0.070017	0.074152	0.076926	0.077814
Cuneus	0.022176	0.023720	0.041287	0.043567	0.098573	0.101249	0.101808	0.100763
Entorhinal Cortex	0.034577	0.034606	0.038569	0.039318	0.098404	0.098808	0.096880	0.093335
Frontal Pole	0.030976	0.030947	0.031354	0.031038	0.091326	0.091963	0.091334	0.089763
Fusiform Cortex	0.030344	0.031186	0.032503	0.033646	0.089951	0.092942	0.094008	0.093824
Hippocampus	0.060475	0.080104	0.077858	0.082498	0.144500	0.153412	0.148966	0.139174
Inferior Temporal Cortex	0.050972	0.048818	0.051360	0.050452	0.143283	0.146495	0.143713	0.136859
Inferior Parietal Cortex	0.038459	0.037379	0.046402	0.044360	0.110860	0.112213	0.111353	0.108831
Insula	0.024867	0.024089	0.025431	0.024546	0.079258	0.078375	0.076880	0.075206
Isthmus of the Cingulate Cortex	0.034847	0.034586	0.039899	0.038784	0.100864	0.101974	0.101535	0.099704
Lateral Occipital Cortex	0.032102	0.032591	0.035414	0.036021	0.096794	0.099786	0.100975	0.100590
Lateral Orbitofrontal Cortex	0.028407	0.029927	0.034749	0.036855	0.088818	0.094928	0.097915	0.097588
Lingual Cortex	0.027162	0.026926	0.029114	0.028677	0.081590	0.082761	0.081900	0.079369
Medial Orbitofrontal Cortex	0.049207	0.049885	0.053069	0.053725	0.118808	0.122216	0.123025	0.121329
Middle Temporal Cortex	0.053286	0.055035	0.065272	0.068883	0.152339	0.168390	0.174367	0.170538
Pallidum	0.038908	0.042774	0.051176	0.055238	0.114477	0.126113	0.134202	0.137437
Paracentral Lobule	0.029615	0.031933	0.036791	0.036754	0.083467	0.087570	0.090991	0.093642
Parahippocampal Cortex	0.020275	0.021219	0.029085	0.030617	0.084519	0.088061	0.090908	0.092993
Pars Opercularis	0.039394	0.043076	0.050488	0.053645	0.106447	0.112813	0.116306	0.116839
Pars Orbitalis	0.028922	0.030317	0.038286	0.038243	0.094722	0.105028	0.113455	0.118398
Pars Triangularis	0.039129	0.037376	0.045394	0.042548	0.110632	0.102675	0.095041	0.088839
Pericalcarine Cortex	0.023395	0.026229	0.031554	0.032233	0.077538	0.082533	0.086710	0.089681
Postcentral Gyrus	0.024306	0.024348	0.026744	0.025483	0.070603	0.070114	0.069175	0.067859
Posterior Cingulate Cortex	0.043809	0.040757	0.046450	0.043123	0.113015	0.107178	0.101541	0.096406
Precentral Gyrus	0.040171	0.045220	0.056943	0.061947	0.111872	0.121621	0.129756	0.134012
Precuneus	0.026947	0.027520	0.028425	0.028415	0.080048	0.081098	0.081095	0.080511
Premotor Cortex	0.003502	0.003642	0.003422	0.003505	0.018270	0.018770	0.019299	0.019820
Putamen	0.036128	0.043096	0.046409	0.051420	0.095324	0.103280	0.109448	0.114578
Rostral Middle Frontal Cortex	0.026615	0.026016	0.029049	0.028027	0.086907	0.085897	0.084460	0.083215
Rostral Anterior Cingulate Cortex	0.017781	0.017555	0.019340	0.018820	0.062054	0.061412	0.060608	0.059938
Superior Parietal Cortex	0.045219	0.043807	0.047278	0.044964	0.112675	0.108341	0.104024	0.099635
Superior Temporal Cortex	0.030010	0.031577	0.041454	0.042978	0.099122	0.105359	0.110735	0.114483
Superior Frontal Cortex	0.025691	0.025860	0.027355	0.027335	0.077345	0.080420	0.082642	0.083567
Supramarginal Gyrus	0.029670	0.031450	0.040708	0.041303	0.089918	0.099520	0.107969	0.113928
Thalamus	0.028427	0.030646	0.036694	0.037359	0.090553	0.095093	0.097983	0.099279
Ventral Diencephalon	0.025255	0.023461	0.029472	0.028045	0.074799	0.075708	0.076546	0.077040

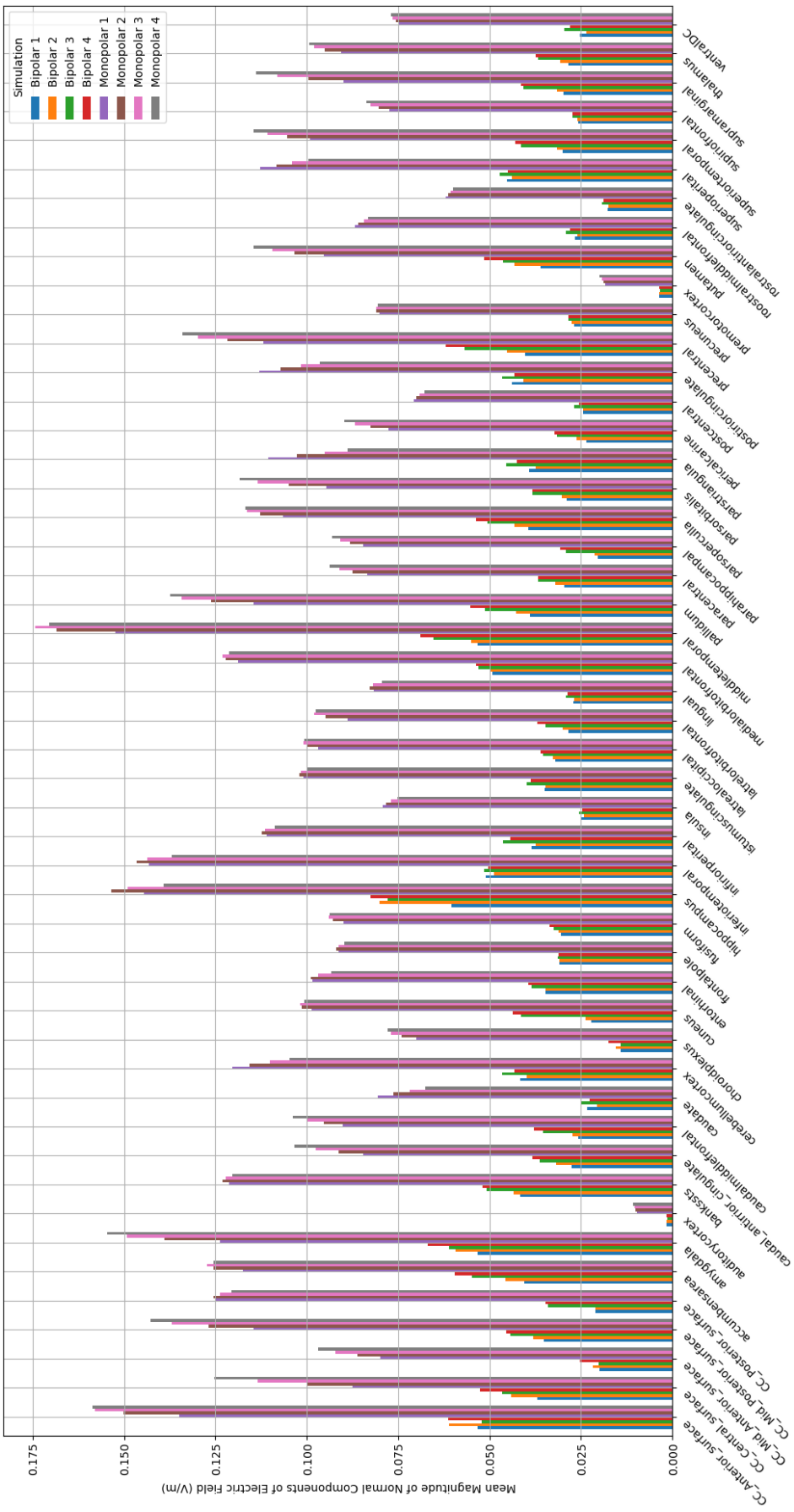

Figure 31: Mean values of the magnitude of normals of EF by Brain Region and Simulation

References

[1] T. L. Davis, D. H. Unwin, J. Jerabek, and B. Roth, "The safety of using body-transmit mri in patients with implanted deep brain stimulation devices," *Movement Disorders*, 2015.

[2] K. A. Sathi and M. K. Hosain, "Modeling and simulation of deep brain stimulation electrodes with various active contacts," *Research on Biomedical Engineering*, vol. 36, pp. 147–161, 2020.

[3] M. Vermaas, M. Piastra, T. Oostendorp, N. Ramsey, and P. Tiesinga, "Femfuns: A volume conduction modeling pipeline that includes resistive, capacitive or dispersive tissue and electrodes," *Neuroinformatics*, vol. 18, 10 2020.

[4] S. M. Gabriel, R. W. Lau, and C. Gabriel, "The dielectric properties of biological tissues: Iii. parametric models for the dielectric spectrum of tissues.," *Physics in medicine and biology*, vol. 41 11, pp. 2271–93, 1996.

[5] Y. Değirmenci, "Current dbs programming," *Deep Brain Stimulation*, vol. 4, pp. 29–31, 2024.

[6] S. Breit, J. Schulz, and A. Benabid, "Deep brain stimulation," *Cell and tissue research*, vol. 318, pp. 275–88, 11 2004.

[7] D. D. Cummins, S. S. Sandoval-Pistorius, S. Cernera, R. Fernandez-Gajardo, L. H. Hammer, and P. A. Starr, "Physiological effects of dual target dbs in an individual with parkinson's disease and a sensing-enabled pulse generator," *Parkinsonism Related Disorders*, vol. 122, p. 106089, 2024.

[8] V. Coenen, F. Amtage, J. Volkmann, and T. Schlaepfer, "Deep brain stimulation in neurological and psychiatric disorders," *Deutsches Ärzteblatt International*, vol. 112, pp. 519–26, 08 2015.

[9] S. Lagerweij, T. van Wieren, M. van Beveren, M. Tijssen, and M. van Egmond, "Dbs for dystonia: Should we take our patients to the swimming pool?," *Parkinsonism Related Disorders*, vol. 96, pp. 36–37, 2022.

[10] B. Van Nieuwenhuyse, R. Raedt, J. Delbeke, W. Wadman, P. Boon, and K. Vonck, "In search of optimal dbs paradigms to treat epilepsy: Bilateral versus unilateral hippocampal stimulation in a rat model for temporal lobe epilepsy," *Brain Stimulation*, vol. 8, no. 2, pp. 192–199, 2015.

[11] M. I. Iacono, S. R. Atefi, L. Mainardi, H. C. Walker, L. M. Angelone, and G. Bonmassar, "A study on the feasibility of the deep brain stimulation (dbs) electrode localization based on scalp electric potential recordings," *Frontiers in Physiology*, vol. 9, p. 1788, Jan 2019.

[12] K. H. Louie, M. N. Petrucci, L. L. Grado, C. Lu, P. J. Tuite, A. G. Lamperski, C. D. MacKinnon, S. E. Cooper, and T. I. Netoff, "Semi-automated approaches to optimize deep brain stimulation parameters in parkinson's disease," *Journal of NeuroEngineering and Rehabilitation*, vol. 18, p. 83, May 2021.

[13] R. Far, I. Saez, A. Sardo, E. Ovruchesky, L. Sperry, L. Zhang, K. Shahlaie, and F. Girgis, "Subthalamic nucleus deep brain stimulation programming settings do not correlate with parkinson's disease severity," *Acta Neurochirurgica*, vol. 164, 06 2022.

[14] K. Palopoli-Trojani, S. L. Schmidt, K. D. Baringer, T. A. Slotkin, J. J. Peters, D. A. Turner, and W. M. Grill, "Temporally non-regular patterns of deep brain stimulation (dbs)

enhance assessment of evoked potentials while maintaining motor symptom management in parkinson's disease (pd)," *Brain Stimulation*, vol. 16, no. 6, pp. 1630–1642, 2023.

[15] S. H. Paek, J. Y. Yun, S. W. Song, I. K. Kim, J. H. Hwang, J. W. Kim, H.-J. Kim, H. J. Kim, Y. E. Kim, Y. H. Lim, M.-R. Kim, J. H. Huh, K. M. Lee, S. K. Park, C. Kim, D. G. Kim, and B. S. Jeon, "The clinical impact of precise electrode positioning in stn dbs on three-year outcomes," *Journal of the Neurological Sciences*, vol. 327, no. 1, pp. 25–31, 2013.

[16] F. Steigerwald, C. Matthies, and J. Volkmann, "Directional deep brain stimulation," *Neurotherapeutics*, vol. 16, no. 1, pp. 100–104, 2019.

[17] P. Fricke, R. Nickl, M. Breun, J. Volkmann, D. Kirsch, R.-I. Ernestus, F. Steigerwald, and C. Matthies, "Directional Leads for Deep Brain Stimulation: Technical Notes and Experiences," *Stereotactic and Functional Neurosurgery*, vol. 99, pp. 305–312, 01 2021.

[18] A. Horn, W.-J. Neumann, K. Degen, G.-H. Schneider, and A. A. Kühn, "Lead placement predicts anatomical targeting errors in subthalamic stimulation for parkinson's disease," *Journal of Neural Engineering*, vol. 15, no. 1, p. 016011, 2018.

[19] M. Keane, S. Deyo, A. Abosch, J. Bajwa, and M. Johnson, "Improved spatial targeting with directionally segmented deep brain stimulation leads for treating essential tremor," *Journal of Neural Engineering*, vol. 9, no. 4, p. 046005, 2012.

[20] S. Treu, B. Strange, S. Oxenford, W.-J. Neumann, A. Kühn, N. Li, and A. Horn, "Deep brain stimulation: Imaging on a group level," *NeuroImage*, vol. 219, p. 117018, 2020.

[21] F. Alonso, P. Zsigmond, and K. Wårdell, "Influence of virchow-robin spaces on the electric field distribution in subthalamic nucleus deep brain stimulation," *Clinical Neurology and Neurosurgery*, vol. 204, p. 106596, 2021.

[22] M. Löffler, I. Cebi, M. Hormozi, M. Synofzik, A. Gharabaghi, and D. Weiss, "Fv 9 deep brain stimulation for targeting tremor and ataxia in sca 27," *Clinical Neurophysiology*, vol. 137, p. e6, 2022.

[23] F. Hell, C. Palleis, J. H. Mehrkens, T. Koeglsperger, and K. Bötzel, "Deep brain stimulation programming 2.0: Future perspectives for target identification and adaptive closed loop stimulation," *Frontiers in Neurology*, vol. 10, p. 314, 2019.

[24] M. D. Johnson, S. Miocinovic, C. C. McIntyre, and J. L. Vitek, "Mechanisms and targets of deep brain stimulation in movement disorders," *Neurotherapeutics*, vol. 5, pp. 294–308, 2008.

[25] G. Deli, I. Balas, F. Nagy, E. Balazs, J. Janszky, S. Komoly, and N. Kovacs, "Comparison of the efficacy of unipolar and bipolar electrode configuration during subthalamic deep brain stimulation," *Parkinsonism Related Disorders*, vol. 17, no. 1, pp. 50–54, 2011.

[26] L. Almeida, P. V. Rawal, B. Ditty, B. L. Smelser, H. Huang, M. S. Okun, B. L. Guthrie, and H. C. Walker, "Deep brain stimulation battery longevity: Comparison of monopolar versus bipolar stimulation modes," *Movement Disorders Clinical Practice*, vol. 3, no. 4, pp. 359–366, 2016.

[27] G. Duffley, D. N. Anderson, J. Vorwerk, A. D. Dorval, and C. R. Butson, "Evaluation of methodologies for computing the deep brain stimulation volume of tissue activated," *Journal of Neural Engineering*, vol. 16, p. 066024, oct 2019.

[28] M. A. Nitsche and W. Paulus, "Excitability changes induced in the human motor cortex by weak transcranial direct current stimulation," *The Journal of Physiology*, vol. 527, no. 3, pp. 633–639, 2000.

[29] M. A. Nitsche, L. G. Cohen, E. M. Wassermann, A. Priori, N. Lang, A. Antal, W. Paulus, F. Hummel, P. S. Boggio, F. Fregni, and A. Pascual-Leone, "Transcranial direct current stimulation: State of the art 2008," *Brain Stimulation*, vol. 1, no. 3, pp. 206–223, 2008.

[30] A. Del Felice, L. Castiglia, E. Formaggio, M. Cattelan, B. Scarpa, P. Manganotti, E. Tenconi, and S. Masiero, "Personalized transcranial alternating current stimulation (tacs) and physical therapy to treat motor and cognitive symptoms in parkinson's disease: A randomized cross-over trial," *NeuroImage: Clinical*, vol. 22, p. 101768, 2019.

[31] F. Kasten and C. Herrmann, "Integrating electric field modeling and neuroimaging to explain inter-individual variability of tacs effects," *Nature Communications*, vol. 10, p. 128, 2019.

[32] S. Oxenford, J. Roediger, C. Neudorfer, L. Milosevic, C. Güttler, P. Spindler, P. Vajkoczy, W.-J. Neumann, A. Kühn, and A. Horn, "Lead-or: A multimodal platform for deep brain stimulation surgery," *eLife*, vol. 11, p. e72929, may 2022.

[33] A. Thielscher, A. Antunes, and G. B. Saturnino, "Field modeling for transcranial magnetic stimulation: A useful tool to understand the physiological effects of tms?," in *2015 37th Annual International Conference of the IEEE Engineering in Medicine and Biology Society (EMBC)*, pp. 222–225, 2015.

[34] O. Puonti, K. Van Leemput, G. B. Saturnino, H. R. Siebner, K. H. Madsen, and A. Thielscher, "Accurate and robust whole-head segmentation from magnetic resonance images for individualized head modeling," *NeuroImage*, vol. 219, p. 117044, 2020.

[35] A. M. Dale, B. Fischl, and M. I. Sereno, "Cortical surface-based analysis: I. segmentation and surface reconstruction," *NeuroImage*, vol. 9, no. 2, pp. 179–194, 1999.

[36] R. S. Desikan, F. Ségonne, B. Fischl, B. T. Quinn, B. C. Dickerson, D. Blacker, R. L. Buckner, A. M. Dale, R. P. Maguire, B. T. Hyman, M. S. Albert, and R. J. Killiany, "An automated labeling system for subdividing the human cerebral cortex on mri scans into gyral based regions of interest," *NeuroImage*, vol. 31, no. 3, pp. 968–980, 2006.

[37] A. Klein and J. Tourville, "101 labeled brain images and a consistent human cortical labeling protocol," *Frontiers in Neuroscience*, vol. 6, 2012.

[38] B. Fischl, "Automatically parcellating the human cerebral cortex," *Cerebral Cortex*, vol. 14, pp. 11–22, 01 2004.

[39] Q. Fang, "iso2mesh: A 3d surface and volumetric mesh generator for matlab/octave," 2024. Accessed: 2024-08-19, URL: https://github.com/fangq/iso2mesh.

[40] A. P. Tran, S. Yan, and Q. Fang, "Improving model-based fnirs analysis using mesh-based anatomical and light-transport models," *bioRxiv*, 2020.

[41] Q. Fang and D. A. Boas, "Tetrahedral mesh generation from volumetric binary and grayscale images," in *Proceedings of the Sixth IEEE International Conference on Symposium on Biomedical Imaging: From Nano to Macro*, ISBI'09, p. 1142–1145, IEEE Press, 2009.

[42] M. Vermaas, M. Piastra, T. Oostendorp, N. Ramsey, and P. Tiesinga, "When to include ecog electrode properties in volume conduction models," *Journal of Neural Engineering*, vol. 17, 08 2020.

[43] K. W. Scangos, C. J. Dougherty, J. T. Evans, P. E. Holtzheimer, and H. S. Mayberg, "Dosing of electrical parameters in deep brain stimulation (dbs) for intractable depression: A review of clinical studies," *Frontiers in Psychiatry*, vol. 9, p. 302, 2018.

[44] L. Liu, J. Zhang, J. Sun, and K. Xu, "Impacts of stimulus parameters and configurations on motor cortex direct electrical stimulation using intrinsic optical imaging: a pilot study," *BioMedical Engineering OnLine*, vol. 21, no. 1, p. 58, 2022.

[45] Y. Guo, L. Zhao, Y. Shi, X. Zhang, S. Du, and F. Wang, "Adaptive weighted robust iterative closest point," *Neurocomputing*, vol. 508, pp. 225–241, 2022.

[46] J. T. Francis, B. J. Gluckman, and S. J. Schiff, "Sensitivity of neurons to weak electric fields," *Journal of Neuroscience*, vol. 23, no. 19, pp. 7255–7261, 2003.

[47] J. Modolo, Y. Denoyer, F. Wendling, and P. Benquet, "Physiological effects of low-magnitude electric fields on brain activity: advances from in vitro, in vivo and in silico models," *Current Opinion in Biomedical Engineering*, vol. 8, pp. 38–44, Dec 2018. Epub 2018 Sep 28.

[48] M. Guidetti, M. Arlotti, T. Bocci, A. M. Bianchi, M. Parazzini, R. Ferrucci, and A. Priori, "Electric fields induced in the brain by transcranial electric stimulation: A review of in vivo recordings," *Biomedicines*, vol. 10, no. 10, 2022.

[49] P. C. Miranda, M. Lomarev, and M. Hallett, "Modeling the current distribution during transcranial direct current stimulation," *Clinical Neurophysiology*, vol. 117, no. 7, pp. 1623–1629, 2006.

[50] U. Pancholi and V. Dave, "Analysis of electric field strengths and focality for healthy and neurologically impaired subjects upon multiple tdcs stimulation protocols," *Research on Biomedical Engineering*, vol. 39, pp. 991–1006, December 2023.